Revision 1

Title

Quantitative measurement of olivine composition in three dimensions using X-ray micro-computed tomography.

Authors

Matthew J. Pankhurst[1,2,3,4†], Nghia T. Vo[5], Alan R. Butcher[6,7], Haili Long[6], Hongchang Wang[7], Sara Nonni[4], Jason Harvey[3], Guðmundur Guðfinnsson[8], Ron Fowler[9], Robert Atwood[4,5], Richard Walshaw[10], and Peter D. Lee[4,11].

[1]Instituto Technológico y de Energías Renovables (ITER), 38900 Granadilla de Abona, Tenerife, Canary Islands, Spain.
[2]Instituto Volcanológico de Canaries (INVOLCAN), 38400 Puerto de la Cruz, Tenerife, Canary Islands, Spain.
[3]School of Earth and Environment, University of Leeds, Leeds, LS2 9JT, UK
[4]Research Complex at Harwell, Rutherford Appleton Laboratories, Didcot, OX11 0FA, UK
[5]Diamond Light Source Ltd., Didcot, OX11 0DE, UK
[6]FEI, Stiklestadveien 1, 7041 Trondheim, Norway
[7]Geological Survey of Finland, Fl-02151 Espoo, Finland
[8]Institute of Earth Sciences, University of Iceland, Reykjavik 101, Iceland
[9]Scientific Computing Department, Science and Technology Facilities Council, Rutherford Appleton Laboratory, Harwell Campus, UK, OX11 0QX
[10]Leeds Electron Microscopy and Spectroscopy Centre, University of Leeds, Leeds, LS2 9JT, UK
[11]Mechanical Engineering, University College London, Gower Street, London, WC1E 6BT

†Corresponding author

Abstract

Olivine is a key constituent in the silicate Earth; its composition and texture informs petrogenetic understanding of numerous rock types. Here we develop a quantitative and reproducible method to measure olivine composition in three dimensions without destructive analysis, meaning full textural context is maintained. The olivine solid solution between forsterite and fayalite was measured using a combination of three-dimensional (3D) X-ray imaging techniques, 2D back scattered electron imaging, and spot-analyses using wavelength dispersive electron probe microanalysis. The linear attenuation coefficient of natural crystals across a range of forsterite content from ~73-91 mol% were confirmed to scale linearly with composition using 53, 60 and 70 kV monochromatic beams at I12-JEEP beamline, Diamond Light Source utilising the helical fly-scan acquisition. A polychromatic X-ray source was used to scan the same crystals, which yielded image contrast equivalent to measuring the mol% of forsterite with an accuracy <1.0 %. X-ray tomography can now provide fully integrated textural and chemical analysis of natural samples containing olivine, which will support 3D and 3D+time petrologic modelling. The study has revealed >3 mm domains within a large crystal of San Carlos forsterite that vary by ~2 Fo mol%. This offers a solution to an outstanding question of inter-laboratory standardisation, and also demonstrates the utility of 3D, non-destructive, chemical measurement. To our knowledge, this study is the first to describe the application of XMT to quantitative chemical measurement across a mineral solid solution. Our approach may be expanded to calculate the chemistry of other mineral systems in 3D, depending upon the number, chemistry and density of end-members.

INTRODUCTION

Combining chemical and textural data from rocks is essential to understand their origins and formation. Integrating these petrologic data means being able to place chemical analyses within spatial context, and vice versa. Conventional chemical analysis, however, or the preparation for it, destroys or modifies spatial context in some way. This study documents an advance in non-destructive, quantitative, determination of composition that maintains full three-dimensional (3D) context, using olivine.

Two-dimensional (2D) data using visible light and electron microscopy has underpinned virtually all study of rocks at the micro-scale. Quantitative measurement using optical properties of minerals have been used to investigate rocks for over 150 years (Sorby, 1858). It has also long been recognised that physical properties, some measurable by optical or X-ray diffraction analyses, can be used to estimate the chemical composition and vice versa (e.g. Jahanbagloo, 1969; Poldervaart, 1950). In more recent decades, electron microscopy has provided higher resolution and more analytical options, yet remains limited to 2D measurement. 2D analysis requires cutting, grinding and polishing of the sample, and thus full spatial context for those observations is lost. Furthermore, the nature of conventional preparation and analysis is comparatively slow and expensive, representing a limitation to the gathering of large datasets.

Motivation and aims

The density of olivine can be calculated from its chemical composition and its linear attenuation of X-rays. It is therefore possible to derive chemical information from X-ray attenuation of olivine. Pankhurst et al. (2014) showed that X-ray microcomputed tomography (XMT) image brightness can be used as a proxy for the composition of olivine. Those authors demonstrated equivalence between electron probe microanalysis (EPMA) and XMT results when comparing population histograms of olivine core compositions and grayscale number from a split sample of tephra. This is a viable approach because olivine is generally a solid solution between Fe and Mg end-members (expressed here as the forsterite content Fo = 100 x Mg/[Mg+Fe+Mn], mineral abbreviations throughout follow Whitney and Evans, 2010). Yet those results, without calibration, are qualitative and relative only. Different X-ray beam energies required by different samples, instrument hardware, environmental conditions and operator choices all contribute to the final image brightness values. Therefore, without calibration, the brightness values from laboratory source XMT are arbitrary and non-reproducible.

In this study, we test the ability to reliably measure the attenuation of the olivine solid solution in a volume, using monochromatic XMT, and extract reproducible, quantitative, chemical information. International standard reference materials (SRMs) are used, as well as other natural olivine crystals. Our primary aims are to; 1) measure the tomogram image brightness of a range of olivine compositions using monochromatic X-ray energy; 2) relate those data to density (ρ) via the linear attenuation coefficient (μ); 3) compare results with ρ, as calculated using EPMA data; 4) investigate the use of a regression line as a calibration function that employs image brightness as a quantitative measure of Fo content in a typical laboratory setting (using polychromatic X-rays).

First we check that the linear attenuation coefficient (μ) for each value of Fo scales linearly with Mg-Fe substitution across a Fo range of special interest in nature (i.e., common in mantle and basaltic rocks), using monochromatic X-ray tomography. We then compare 3D image data from laboratory (polychromatic) sources, in order to estimate an uncertainty that can be used to determine the core compositions of large numbers of crystals using scan times of <1 hour. Finally, we investigate the use of X-ray tomography to provide quantitative 3D chemistry on scales useful for petrogenetic modelling of crystal margins.

Olivine occurrence and importance

Measuring the chemistry of olivine $(Mg,Fe)_2SiO_4$ provides insight to its formation, and relationship with its host rock. Olivine is one of the most important minerals on Earth. It is the most abundant mineral in the upper mantle and mediates mantle rheology, density, heat flow and melting (Holtzman et al., 2003; Mizukami et al., 2004). Olivine is also an important component of several meteorite classes and contain clues as to their evolution (e.g. Rudraswami et al., 2016) as well as being a rock-forming mineral present in planetary and satellite bodies .

Olivine is a rock-forming mineral in ultra-mafic to mafic magmas. It also occurs in some felsic and hybridised magmas, and can be indicative of mantle-derived magma input to volcanic systems; frequently implicated as an eruption trigger (e.g. Sigmundsson et al., 2010; Sparks et al., 1977). In these systems, olivine can occur across a considerable composition range, as well as preserving major element chemical zonation within individual grains (Kahl et al., 2013). These observations are leading to new insights as to the origin, dynamics and timescales of magmatic plumbing systems (Hartley et al., 2016; Pankhurst et al., 2018a). In order to make better sense of these often highly complex mineralogical records, large datasets that integrate crystal texture and chemistry are required.

The most common substitution in olivine is that between 2^+ cations in the M sites. Iron exchange for Mg is accompanied by a disproportionately large change in the molecular mass of the unit cell with respect to its volume change (Deer et al., 1992). Accordingly, Fo (Mg end-member: $\rho = 3.22$) is ~26.5% less dense than fayalite (Fa; Fe end-member: $\rho = 4.29$), which is the property we exploit here with X-ray imaging. Since electron density is equitable to proton density for a given solid solution, XMT images of olivine appear much like back-scattered electron (BSE) images, which are a measure of atomic density (Z contrast). Thus, we can use state-of-the-art 2D BSE imaging as a useful method of validating the 3D image data.

3D data and X-ray microtomography

Full three-dimensional (3D) data from natural samples offers the advantage that measurement of volume distributions, distances between features and shape descriptors can be conducted directly. Non-destructive 3D data also has advantages for observing large volumes of material to find and target rare features, as well as providing context for destructive in-situ measurements. Obtaining accurate 3D, non-destructive, data from what are (in almost every case) opaque materials, however, is only possible with tomographic techniques using X-rays, neutrons and muons (Cnudde and Boone, 2013; Marteau et al., 2012; Winkler et al., 2002).

Gathering three dimensional (3D) data at the micro-scale has progressively become more routine in geological research. Crystallographic orientation and boundary data has traditionally been obtained from thin sections by using universal stages on petrographic microscopes (see Kile, 2009 for a review). Serial sectioning and well-constrained extrapolation has been used to place measurements into 3D context across cm scales (Bryon et al., 1995; Cooper and Hunter, 1995). X-ray computed tomographic imaging (Flannery et al., 1987) provides full 3D data (e.g. Denison and Carlson, 1997; Philpotts et al., 1999). Centimetre to nanometre resolution X-ray imaging has become increasingly utilised (Cnudde and Boone, 2013; Ma et al., 2016; Macente et al., 2017; Suuronen and Sayab, 2018). To date, XMT has been used mainly to recover rock textures (e.g. Cnudde and Boone, 2013; Fonseca et al., 2013; Jerram et al., 2009; Ketcham, 2005; Mock and Jerram, 2005), and mineralogy (Lemelle et al., 2004), phase size distributions and their evolution (Hall et al., 2010; Ketcham and Carlson, 2001; Lin et al., 2016; Reyes et al., 2017), and dynamic processes such as diffusion through porous rocks (Nakashima, 2000). For a thorough introduction to XMT applications in geosciences we refer the reader to Cnudde and Boone (2013), and in more detail as applied to igneous texture see (Jerram et al., 2018 and references therein). A key advantage of XMT is the very high rate of data acquisition that is possible, which can support efforts to build large datasets efficiently (Pankhurst et al., 2014), and would otherwise rely on time-intensive analysis.

The transmission of X-rays through a rock depends upon minerals' chemistry and density, the thickness of the sample, and the energy of the X-ray beam. X-rays are attenuated by electrons, limiting the number of photons arriving at the detector (see Pankhurst et al., 2018b for an introduction and key references). Contrasts in these properties (and thus electron density) throughout a sample attenuate an X-ray beam to different degrees, producing differences in detector response. These responses are recorded as image brightness values.

If a reproducible set of beam conditions and settings are used, the values can be directly compared within and across datasets. For instance, in the case of samples containing one mineral, if the X-ray energy and linear attenuation coefficient is known, sample thickness can be measured (Anderson et al., 1998). To map composition in 3D, 2D projections acquired around a sample (normally the sample is rotated) are tomographically reconstructed; voxel brightness of the resulting tomographic image can be used to identify different phases (Leber et al., 2004) and the concentration of certain phases (Yue et al., 2011).

METHODS

Samples

Samples were selected to provide a useful range of natural occurring olivine at the forsteritic end of the solid solution (~Fo_{70-90}); those compositions dominate olivine occurring in mantle and basaltic rocks. Intermediate to comparatively evolved olivine (Fo_{30-70}) is less abundant in nature and could not be obtained in large enough grain sizes; measuring these compositions is planned for further work at higher resolution. The fayalite end member was nevertheless available. Thus the sample set contains both a wide spread of compositions, albeit with a higher data density around the most commonly occurring range Fo_{70-90}.

Rock samples Killbourne Hole Peridotite (New Mexico, USA), Picrite from Háleyjarbunga lava shield (Iceland) and an alkali basalt from Papua New Guinea (Star-1) were coarsely crushed. A large (~2 cm) forsterite crystal from the locality of San Carlos, New Mexico, and part of a large (~4 cm) piece of fayalite from Rockport, Mass (USA), were also coarsely crushed. Olivine was handpicked under a binocular microscope from the crushed material, and from some tephra samples (flank and summit samples from the 2010 Eyjafjallajökull) and sand from a green beach from Hawaii (legacy sample from Papakōlea). We direct the reader to Fig. 1 for a description of how the olivine was mounted for analysis. Not all samples are discussed further; those indicated in Table 1 with an asterisk were used in the calibration. The remaining samples imaged as part of the stack provides calibrated material for use in future work.

Preparation for integrated 1, 2 and 3D measurement

Olivine crystals were prepared by setting them in resin discs in order for them to cut, polished and analysed after the non-destructive XMT scans. This shape minimises the use of vertical field of view, and the flat upper and lower surfaces afford a stable platform on which to mount other material, which allows for ready insertion in later experiments (i.e. as internal standards). The diameter (14 mm) is suitable for re-use in laboratory XMT experiments in which <10 µm pixel resolution is desirable.

Each disc was composed of a single layer of crystals, set in place using a two-part epoxy resin (Epothin®) using a soft plastic pipette tube as a mould (Fig. 1). The low initial viscosity of Epothin® wet olivine surfaces and limited the entrapment of air bubbles. The discs were then flattened with sandpaper to reduce the height of each to a minimum while still containing all the grains. Each disc was then labelled using an engraver (removal of resin means the label can be read in the X-ray images). A stack of the discs was made using double-sided tape, and was then mounted upon a resin pedestal made from the neck section of the pipette (Fig. 2).

Legacy olivine crystal mounts from Pankhurst et al. (2014) were cut down to ~1 cm^2, ~1 mm thick chips using a combination of a Buehler PetroThin® thin-sectioning system, and a single edged razor blade. These pre-analysed crystals serve as secondary internal standards across a useful Fo range. The cores of these crystals are known to be homogenous from previous BSE imaging and EPMA data (Pankhurst et al., 2018a). The group of chips are labelled as one position in Fig. 1, see Table 1.

X-ray micro-tomography imaging: monochromatic source

To confirm that the relationship between linear attenuation and Fo-Fa solid solution is linear at a number of single energies, monochromatic X-ray beams were used. The olivine stack was imaged using 53, 60 and 70 kV beams at the Joint Engineering, Environmental and Processing (JEEP) beamline (i12; see Drakopoulos et al., 2015) at the Diamond Light Source Ltd., United Kingdom, to gather absorption image data at each single energy. These energies are typical of peak polychromatic beams used in laboratory X-ray sources to image igneous rocks up to a thickness of ~2 cm (e.g. Reyes-Dávila et al., 2016), which corresponds to the scale of a thin section. Camera module 2 was used which has a magnification of 0.82, a field of view of 20.3 mm in the horizontal and 15 mm usable in the vertical (per projection), with a pixel resolution of 7.9 µm. A continuous helical scan-track (with a pitch of 10 mm) was used to collect projection data from the stack of samples in one scan. This allowed the entire sample to be imaged without increasing the horizontal field of view, which would have decreased resolution. In addition, this scan mode helps to significantly reduce ring artefacts within the reconstructed images (caused by the fixed defective regions on the detector). The raw projections were then pre-processed using the following techniques: (1) sinogram generation, which extracts tilted slices through the 3D helical datasets depending on the helical pitch; (2) zinger removal (Rivers, 1998), which removes artificial bright lines; (3) blob removal, which reduces the impact of dead region(s) on the detector; (4) ring removal, to clean up small ring artefacts that may remain (Vo et al., in prep); (5) center of rotation calculation (Vo et al., 2014). Finally, the volume was reconstructed by filtered back-projection (FBP; Ramachandran and Lakshminarayanan, 1971). All techniques are implemented in python codes (using h5py, scipy, numpy, pyfftw, and pyCUDA) by N. Vo.

X-ray micro-tomography imaging: polychromatic sources

The purpose of using a polychromatic beam from a non-synchrotron source was to provide a guide to the potential accuracy and precision of olivine chemical composition that can be achieved using an instrument common in many research environments. The stack was scanned using an FEI HeliScan system in Trondheim, Norway. Proprietary software was used to correct subtle beam hardening, which was largely avoided due to the high angle scanning approach. Data was supplied in 16-bit tiff format. Samples within the stack were also (circular) scanned at the Research Complex at Harwell using a Nikon 225 XTH system, using the polychromatic beam characterisation procedure described in Pankhurst et al. (2018b) to correct for beam hardening at specified density values (i.e. density of 3.35 g/cm^3 for the disc containing shards of olivine from San Carlos).

2D imaging and 1D chemical analysis

Selected resin discs were prepared for electron probe microanalysis using standard materials (see Fig. 2 for analytical workflow). A JEOL electron probe micro-analyser (EPMA) 8320 Superprobe with five wavelength-dispersive (WD) spectrometers housed at the University of Leeds Electron Microscopy and Spectroscopy Centre was used to collect high resolution and high contrast backscattered electron (BSE) images. Brightness and contrast settings, which are normally adjusted according to user subjectivity and according to the feature of interest in each frame, were instead tuned to internal reference materials (San Carlos olivine: near detection limit; Fe-oxide; near saturation). EPMA spots (nominally 1 µm size) were measured at the University of Iceland with the setup described in Pankhurst et al. (2017). While colourgreater precision is able to be achieved using wider beams, higher current and longer analysis times, we wished to compare the XMT results with typical EPMA settings for olivine. Smithsonian Institute (Washington D.C., USA) distributed micro-beam reference materials (RM) San Carlos Olivine (NMNH 111312-44) and Springwater Meteorite Olivine (USNM 2566) were used as primary and secondary RMs respectively.

The Springwater Meteorite RM returns precise major and minor oxide concentrations when run as a secondary standard (see Table 2). No significant drift was detected through the run, and as such we assign a maximum 2σ uncertainty to each position of ±0.25 mol % Fo.

Building a calibration between techniques

Positions of EPMA spot analyses were precisely located on BSE images in order to calibrate composition with BSE grayscale brightness, following the approach of Pankhurst (2018a). First, the BSE images were assessed using a variety of lookup tables in ImageJ (Rasband, 2015) to confirm homogeneity of the crystal cores or shards. Circles of 10 µm diameter were located in regions of constant grayscale, which were then measured and deleted from the image to form a white 'target'. Using the software CrossHair v1.1 (Lin, 2007), these spots could be co-located with high spatial accuracy using the JEOL interface, which also employs a crosshair location option. Two or three spot analyses were taken from the 10 µm diameter position, in the core of each crystal or shard, and averaged. Thus, an appropriate level of spatial accuracy that links the chemical and image data was attained.

Optical microscope work and BSE images helped identify the locations of chemical spot analyses in the 3D images. These locations were checked for intensity gradients before values were recorded using ImageJ, using circular regions ~100 µm in diameter, recording the mean and standard deviation. We applied a non-local mean filter to the data for presentation purposes, but report all grayscale and 2σ values after applying a 2-pixel median filter, which is well below the sampling resolution, yet necessary to minimise noise. It should be noted that it is possible to frame average using numerous projections at each angle. This would have the same effect (at least for the purpose here, since we do not ascribe meaning to features less than 5 pixels), yet would take almost an order of magnitude more instrument time to achieve the same image quality. The location reproducibility between 3D images is estimated at <10 µm in XY and <20 µm in Z, which is well below the voxel sampling resolution.

Density calculations using X-ray attenuation

Linear attention of olivine end-members at different X-ray energies were calculated using the National Institute of Standards and Technology Physical Measurement Laboratory Database; https://physics.nist.gov/PhysRefData/Xcom/html/xcom1.html. Results from this database are reported as mass attenuation coefficients, from which linear attenuation is derived simply as a function of material density. Density values from Deer et al. (1982) were used and can be considered to scale as a linear function of composition (Bloss, 1952) across the range of interest here (Fo73-91). Thus attenuation is also predicted to be linear as a function of composition (Fig. 5). Values from online calculations are reported in the supplementary Table S1.

Calculations here assume a perfect solid solution between forsterite and fayalite, since tephroite (Tep; Mn end-member) is present only up to a few percent and has very similar density to fayalite. All other end members are in low enough abundance to warrant this assumption to a first order in typical igneous rocks (e.g. monticellite is rarely above half a percent). Values are expressed as Fo mol %, and implies the remainder is comprised of Fa and Tep.

RESULTS

Linear attenuation as measured by monochromatic X-rays, or image brightness values from polychromatic X-rays were extracted from tomograms and are presented in Table 3. The quality of the fayalite sample images was poor in comparison to the forsteritic samples; streak artefacts are evident (see Supplementary Figure 1).This is reflected in the considerable spread of linear attenuation values at constant chemical composition (Fo0).

Homogeneous brightness levels are observed in the cores of crystals in both polychromatic and backscatter electron image data (Fig. 3). The fayalite sample is the exception, this sample was too attenuating to be imaged satisfactorily (while using the same beam conditions as the rest of the stack). Relative image brightness (i.e. grayscale level) is in good qualitative agreement between the two (compare Fig. 3b i to iii and ii to iv).

Example calculations of linear attenuation according to solid solution chemistry are presented in the supplement, as are full EPMA results. Each tomographic image dataset is several gigabytes in size; we illustrate selected potions of these data as renders and slices in Figs 3 and 4, including comparisons to BSE images. Calibration of image data with chemical composition is illustrated in Figs. 5 and 6.

DISCUSSION

Relationship between linear attenuation and composition

Densitometric calculations predict that the olivine solid solution can be considered linear in the Fo73-91 range. Compositions measured by EPMA and linear attenuation (μ) are well correlated ($R^2 > 0.9$) at the three monochromatic energies (Fig. 5). It is likely that the particle size used for the fayalite (chosen to match the less dense, more forsteritic, samples) did not allow comparable transmission. This explains why, in addition to the wide spread of linear attenuation values, the average linear attenuation value for fayalite is slightly lower than that predicted from the Fo73-91 array.

Discrepancy is also observed between calculated and measured μ at any given position along the solid solution; the measured attenuation is lower than expected. This may be due to a scaling effect in detector response, although it is possible that the cause is associated with a property of the crystals themselves (i.e. leading to higher transmission than anticipated). While the measured and calculated trends do not match, their relative positions as a function of kV is the same. Whether this offset is a function of the imaging setup or reflective of a physical property of olivine, neither poses a barrier for the practical application developed below. Current work is being undertaken to resolve why this offset occurs.

An advance in measuring chemistry using quantitative densitometry

Retrieving quantitative and reproducible image data of materials using polychromatic X-ray micro-computed tomography systems is an active field of research. The original technique was designed to provide qualitative information in medical and materials research in 3D, and thus instrument drift, optical and digital artefacts and scintillator degradation did not inhibit the collection of meaningful data. In contrast, these issues must be mitigated against to achieve useful, reproducible, quantitative image data.

Davis et al. (2015) showed that by first characterising a polychromatic beam using a step wedge, and then using a virtual phantom of the material of interest, a beam hardening correction could be derived. Then, the quantitative density distribution of simple materials could be calculated in 3D. While those authors' motivation was partly to map the mineral density of teeth, the approach is the same as ours. Rather than air 'diluting' the electron density of a single substance via a texture, we are measuring the relative proportions of end-member composition along a single solid solution, with a unique chemical result for a given density.

Helical scan data returns a linear fit to Fo content of crystal cores (Fig. 6a), and is shown to return higher precision (derived simply from image noise) than the synchrotron data. We reiterate that our intention was not to compare precision between monochromatic and polychromatic beams; increasing the length of each scan would result in higher signal:noise. The important result is that laboratory systems are shown produce at least the same quantitative measurement for olivine crystal cores in <1 hour than can be achieved with a synchrotron source in <10 min at 53 kV. The comparison is shown simply to demonstrate that laboratory source systems offer a practical and accessible solution to the construction of very large, quantitative, olivine crystal core datasets that have acceptable precision and accuracy with which to compare populations of crystals. Laboratory scans can be externally calibration using the procedures of Pankhurst et al. (2018b) and/or by using internal olivine standards.

In this study we have proven that within analytical uncertainty, the olivine solid solution has a linear response to both X-ray energy and Fo content in the range Fo_{73-91}. The degree of variation in attenuation evident at the same composition may be due to crystallographic effects, although more study is required to resolve this question. This means that 3D chemical relationships between individual grains can be recovered using the attenuation of monochromatic and polychromatic X-ray beams.

Present advantages and limitations

A practical advantage of laboratory systems is that image resolution is scales with the field of view due to the conical beam shape. Reducing the distance between the sample and source improves the resolution. With a smooth 'zoom', the resolution can be optimised to the scale of interest. At synchrotron facilities that use a parallel beam, image resolution is essentially fixed by the camera module at any sample distance. Finally, the rapid developments in laboratory-source X-ray imaging systems, in particular improvements in electron gun stability, offer greatly enhanced reproducibility than earlier generations. Like any comparative technique, the use of internal standards is essential for calculating uncertainty, regardless of whether synchrotron or laboratory sources are used. Unlike EPMA, however, the standards and samples can be measured simultaneously (i.e. in the same field of view), which bypasses drift correction.

At crystal margins, where chemical zonation is both common and shown to contain valuable temporal information (e.g. Hartley et al., 2016; Pankhurst et al., 2018a), the comparison between BSE and laboratory X-ray images is encouraging, yet not sufficient at the resolution in the present study to retrieve quantitative data within ~100 µm from the crystal rim with comparable accuracy to EPMA (see Fig. 3). This is likely due to subtle beam hardening effects which are non-linear in regard to material composition, and also depend upon the region of interest's position in the sample itself. Method development to overcome these final limitations for application, for example, element diffusion modelling, is currently being researched. Optimisation techniques could combine 1) pre-filtering a polychromatic beam while retaining useful image contrast, 2) use of analogue phantoms of homogeneous composition that bracket that of the sample density in conjunction with 3) collecting beam intensity data (Pankhurst et al. 2018b) which would allow a researcher to tune beam-hardening correction factors *a posteriori* using (2) as monitors of beam hardening effects.

San Carlos Olivine compositional variation

The potential for some compositional mismatch between our olivine from San Carlos to that of the San Carlos SRM was anticipated from inter-laboratory comparisons using Smithsonian and non-Smithsonian material (Fournelle, 2011). Nevertheless, our results were unexpected. Despite originating from a single crystal, two distinct compositions were observed in the XMT data (Fig. 7). Each shards' grouping is corroborated by the BSE, EPMA and laboratory XMT data. Most shards are composed of Fo90.9, yet four pieces are slightly more evolved; all returning Fo89.1. This demonstrates that extremely subtle differences in olivine chemistry can be resolved by XMT.

Each shard appeared to be homogeneous in BSE intensity across each shard is either flat or contains gradients corresponding to Fo variation far less than our EPMA uncertainty. These subtle gradients could be due to real variation, or a function of preparation. There is no relationship with Z distance (determined using the autofocus feature of the probe for EPMA software; Donovan et al., 2012), and the subtle tilt of the polished surface is unlikely to explain such gradients. It is conceivable that BSE signal intensity could be mediated by crystal orientation, yet if this was the case, and in a population of 11 randomly oriented shards, we should expect a spread of values rather than two distinct groups. Differences in polishing or perhaps even stage position (which might indicate an electrical bias in the chamber) can also be ruled out; the groupings are not spatially related. EPMA profiling including trace element mapping, and determination of crystallographic orientation, is planned for these shards, which may resolve these questions. The simplest explanation is that this single large crystal is zoned and comprised of distinct domains with relatively sharp boundaries between them. Further XMT work is planned for complete crystals.

Fournelle (2011) reported values across a range between ~Fo_{88} to $Fo_{91.5}$ for non-USNM San Carlos olivine, with the highest peak at $Fo_{90.9}$ (Fig. 7). This composition corresponds to the group with the largest number of shards (group 2), and is consistent with a homogeneous core that dominates the volume of a crystal. The sub-dominant group 1 could be explained as being derived from a slightly more evolved overgrowth or diffusion rim, which is almost ubiquitous in volcanic olivine (e.g. Hartley et al., 2016; Kahl et al., 2011). The accepted value of USNM San Carlos Olivine is based on what is a comparatively tiny volume of crushed material which, intriguingly, sits between the two "extremes" (Fournelle, 2011).

Investigating 3D chemistry and texture without a linking step

Reconciling textural information with chemical data continues to drive petrologic research, and is an essential feature in any viable petrogenetic model. When measuring in 2D, however, there is always some potential for chemical data to be mis-located in terms of its textural context. For example, the middle of a crystal in 2D is not necessarily its core. A measurement 100 µm from a crystal rim in 2D could be less in 3D. Thus 2D measurements of texture and chemistry provide the potential to integrate information at a population level only (e.g. Morgan and Jerram, 2006). This is because what is measured from individual grains cannot be directly carried over to the third dimension due to these sectioning effects at the single-grain scale. Good representation is usually achieved simply by measuring over a wide enough area to capture a statistically meaningful dataset, yet these statistics do not provide context at the scale of individual grains. To link two-dimensional mineralogical observations to dynamic, physical processes that occur in three dimensions either some form of careful stereoscopic correction, extrapolation or reasoned assumption in regard to the third direction must be made (e.g. Morgan and Jerram, 2006). Current work is investigating olivine chemistry and size in natural rocks that contain other minerals.

In comparatively simple cases this does not preclude robust conclusions to be formed. However, since crystals can have complex histories (Kahl et al., 2013), population trends may not accurately reflect bulk magma behaviour or history. Technology that *inherently* links direct textural and chemical measurements overcomes the issue, since integration can be conducted at the grain scale. To aid definition of grain boundaries in samples that contain phases with similar attenuation to that of olivine, multiple X-ray tomographic techniques such as phase contrast imaging (Wang et al., in press; Wang et al., 2016a, b) can be used. Crystallographic orientation can also be determined using XMT (McDonald et al., 2015), which raises the possibility of extracting 3D maps of Fo content that are fully integrated with diffusion anisotropy for individual crystallographic domains.

Since these data are quantitative and reproducible, they are poised to address questions requiring fully integrated spatial and chemical context in 3D, and in in-situ experiments: 3D plus time (see Alvarez-Murga et al., 2017; Baker et al., 2012; Cai et al., 2014; Pistone et al., 2015). Monochromatic X-ray beams ≤53 kV are recommended to measure variation within single crystals to achieve enhanced contrasts (reducing uncertainty further) and to avoid beam hardening effects (compare the 53 with the 70 kV data in Fig. 5). The use of dual-energy laboratory X-ray systems (Liu et al., 2009) in geological research will likely allow quantitative 3D chemical measurement of mineral systems with three dominant end-members, such as pyroxene and feldspar.

XMT provides useful spatial context for the characterisation of new, and possibly existing, natural micro-beam standards. Such material must be homogeneous by definition. XMT provides a rapid method to determine how suitable a material might be, before comparatively more laborious analysis is conducted.

Quantitative X-ray micro-tomography can now provide raw data to further improve diffusion models (see Shea et al., 2015), targeting for in-situ Fe-Mg isotope analysis (Sio et al., 2013), and place such observations within full 3D textural analysis of olivine, which itself contains vital evidence for petrogenetic processes (Erdmann et al., 2014; Vinet and Higgins, 2011). With measurements of the volume, density and shape of crystals, physical behaviour (such as settling velocity) can be explored, and related back to chemical records in those crystals. Linking these insights will underpin developments such as determining dynamic processes in sills (e.g. Egorova and Latypov, 2013; Gibb and Henderson, 1992; Holness et al., 2017) crystal mushes (e.g. Thomson and Maclennan, 2013), and piecing together volcanic plumbing system behaviour (Pankhurst et al., 2018a).

Where a significant mass (10s to 100s mg) of olivine grains are required for isotopic measurements, checking an entire population of grains before chemical digestion can be difficult. Peridotite xenoliths, while not necessarily preserving direct evidence for melt-rock interaction in the form of, for example, pyroxenite veins, may still preserve cryptic metasomatic effects of this process distal from the location of the pyroxenite itself. Screening olivine grains in crushed peridotite for chemical zoning derived from melt-rock interaction prior to digestion would be one such use of this technique. Another is obtaining 3D chemical information of olivine in-situ, providing context of such processes involved in the deposition, removal, and modification of accessory phases (Harvey et al., 2015).

There are a number of emergent “non-traditional” stable isotope systems where, as mass spectrometer sensitivity continues to improve, the transition from bulk-rock to mineral aggregate measurements, and toward single-grain and sub-grain measurement (Sio et al., 2013) will inevitably progress. Olivine is already of particular interest for Mg isotope studies (Chaussidon et al., 2017), and bulk-rock isotopic measurements of Fe (e.g. Huang et al., 2011), Ni (e.g. Gall et al., 2017) and Cr (e.g. Farkaš et al., 2013) are the vanguard for similar measurements on olivine aggregates. The proliferation of mass spectrometer amplifiers that can precisely record beam intensities of a few millivolts will mean that olivine mineral separates, demonstrably free of metasomatic effects prior to chemical preparation, will be critical for these applications.

IMPLICATIONS AND APPLICATIONS OF 3D CHEMICAL MEASUREMENT OF OLIVINE

Calibrated 3D X-ray images now can contain spatial and chemical information per voxel. A number of key advances are now possible:

- Crystal chemical populations can be fully integrated with size distributions, textural features and spatial relationships. These data will help unravel complex petrogenetic relationships in particular.
- Samples of extreme value can be chemically analysed using a non-destructive method.
- Composition can be tracked in 3D-plus-time during in-situ experiments.
- 3D olivine growth, dissolution and diffusion models can be tested using natural 3D data.
- Olivine separates can be screened for metasomatic effects prior to digestion and isotopic analysis.
- Microbeam standards can be screened for major element heterogeneity (entire existing mounts or material prior to mounting), and potentially reduce analytical inaccuracy due to standard inhomogeneity.

ACKNOWLEDGEMENTS

This work was conducted under the auspices of an AXA Research Fund Fellowship to MJP and NERC grant (UK) grant NE/M013561/1. Synchrotron tomography was undertaken on I12 at Diamond Light Source under proposals EE14033-1 and EE14033-2. The British Natural History Museum, Thor Thordarson, Godfrey Fitton, Michael Turner and Iain Smith are gratefully acknowledged for providing samples of olivine and/or olivine-rich naturally occurring rocks. Tom Shea and Tomoaki Morishita are thanked for their thoughtful and thorough reviews which improved the manuscript. Julia Hammer is thanked for her editorial handling.

DATA STATEMENT

Representative samples of the research data are shown in the figures. Other datasets generated during and/or analysed during this study are not publicly available due to their large size but are available from the corresponding author on reasonable request.

REFERENCES

Alvarez-Murga, M., Perrillat, J. P., Le Godec, Y., Bergame, F., Philippe, J., King, A., Guignot, N., Mezouar, M., and Hodeau, J. L., 2017, Development of synchrotron X-ray micro-tomography under extreme conditions of pressure and temperature: Journal of Synchrotron Radiation, v. 24, no. 1, p. 240-247.

Anderson, P., Levinkind, M., and Elliott, J. C., 1998, Scanning microradiographic studies of rates of in vitro demineralization in human and bovine dental enamel: Archives of Oral Biology, v. 43, no. 8, p. 649-656.

Baker, D. R., Brun, F., O'Shaughnessy, C., Mancini, L., Fife, J. L., and Rivers, M., 2012, A four-dimensional X-ray tomographic microscopy study of bubble growth in basaltic foam: Nature Communications, v. 3, p. 1135.

Berger, M. J., Hubbell, J., Seltzer, S., Chang, J., Coursey, J., Sukumar, R., Zucker, D., and Olsen, K., 2016, XCOM: Photon cross sections database, NIST Standard reference database, Volume 8, p. 3587-3597.

Bloss, F., 1952, Relationship between density and composition in mol per-cent for some solid solution series: American Mineralogist, v. 37, no. 11-1, p. 966-981.

Bryon, D., Atherton, M., and Hunter, R., 1995, The interpretation of granitic textures from serial thin sectioning, image analysis and three-dimensional reconstruction: Mineralogical Magazine, v. 59, no. 2, p. 203-211.

Cai, B., Karagadde, S., Yuan, L., Marrow, T. J., Connolley, T., and Lee, P. D., 2014, In situ synchrotron tomographic quantification of granular and intragranular deformation during semi-solid compression of an equiaxed dendritic Al-Cu alloy: Acta Materialia, v. 76, p. 371-380.

Chaussidon, M., Deng, Z., Villeneuve, J., Moureau, J., Watson, B., Richter, F., and Moynier, F., 2017, In Situ Analysis of Non-Traditional Isotopes by SIMS and LA–MC–ICP–MS: Key Aspects and the Example of Mg Isotopes in Olivines and Silicate Glasses: Reviews in Mineralogy and Geochemistry, v. 82, no. 1, p. 127-163.

Cnudde, V., and Boone, M. N., 2013, High-resolution X-ray computed tomography in geosciences: A review of the current technology and applications: Earth-Science Reviews, v. 123, no. 0, p. 1-17.

Cooper, M. R., and Hunter, R. H., 1995, Precision serial lapping, imaging and threedimensional reconstruction of minus-cement and post-cementation intergranular pore-systems in the Penrith Sandstone of north-western England: Mineralogical Magazine, v. 59, no. 2, p. 213-220.

Davis, G. R., Evershed, A. N. Z., and Mills, D., 2015, Characterisation of materials: determining density using X-ray microtomography: Materials and Science and Technology, v. 31, no. 2, p. 162-166.

Deer, W., Howie. RA, and Zussman, J., 1982, Rock-forming minerals. vol. 1 A; orthosilicates, Longman, UK, 919p.

Deer, W. A., Howie, R. A., and Zussman, J., 1992, An introduction to the rock-forming minerals, Longman London.

Denison, C., and Carlson, W. D., 1997, Three-dimensional quantitative textural analysis of metamorphic rocks using high-resolution computed X-ray tomography: Part II. Application to natural samples: Journal of Metamorphic Geology, v. 15, no. 1, p. 45-57.

Donovan, J., Kremser, D., and Fournelle, J., 2012, Probe for EPMA: acquisition, automation and analysis: Probe Software, Inc., Eugene, Oregon.

Drakopoulos, M., Connolley, T., Reinhard, C., Atwood, R., Magdysyuk, O., Vo, N., Hart, M., Connor, L., Humphreys, B., and Howell, G., 2015, I12: The joint engineering, environment and processing (JEEP) beamline at diamond light source: Journal of Synchrotron Radiation, v. 22, no. 3, p. 828-838.

Egorova, V., and Latypov, R., 2013, Mafic–Ultramafic Sills: New Insights from M- and S-shaped Mineral and Whole-rock Compositional Profiles: Journal of Petrology, v. 54, no. 10, p. 2155-2191.

Erdmann, S., Scaillet, B., Martel, C., and Cadoux, A., 2014, Characteristic Textures of Recrystallized, Peritectic, and Primary Magmatic Olivine in Experimental Samples and Natural Volcanic Rocks: Journal of Petrology, v. 55, no. 12, p. 2377-2402.

Farkaš, J., Chrastný, V., Novák, M., Čadkova, E., Pašava, J., Chakrabarti, R., Jacobsen, S. B., Ackerman, L., and Bullen, T. D., 2013, Chromium isotope variations (δ 53/52 Cr) in mantle-derived sources and their weathering products: Implications for environmental studies and the evolution of δ 53/52 Cr in the Earth’s mantle over geologic time: Geochimica et Cosmochimica Acta, v. 123, p. 74-92.

Flannery, B. P., Deckman, H. W., Roberge, W. G., and D'Amico, K. L., 1987, Three-Dimensional X-Ray Microtomography: Science, v. 237, no. 4821, p. 1439-1444.

Fonseca, J., O'Sullivan, C., Coop, M. R., and Lee, P. D., 2013, Quantifying the evolution of soil fabric during shearing using directional parameters: Geotechnique, v. 63, no. 6, p. 487-499.

Fournelle, J., 2011, An Investigation of “San Carlos Olivine”: Comparing USNM-distributed Material with Commercially Available Material: Microscopy and Microanalysis, v. 17, no. SupplementS2, p. 842-843.

Gall, L., Williams, H. M., Halliday, A. N., and Kerr, A. C., 2017, Nickel isotopic composition of the mantle: Geochimica et Cosmochimica Acta, v. 199, p. 196-209.

Gibb, F. G. F., and Henderson, c. M. B., 1992, Convection and crystal settling in sills: Contributions to Mineralogy and Petrology, v. 109, no. 4, p. 538-545.

Hall, S., Bornert, M., Desrues, J., Pannier, Y., Lenoir, N., Viggiani, G., and Bésuelle, P., 2010, Discrete and continuum analysis of localised deformation in sand using X-ray µCT and volumetric digital image correlation: Géotechnique, v. 60, no. 5, p. 315-322.

Hartley, M. E., Morgan, D. J., Maclennan, J., Edmonds, M., and Thordarson, T., 2016, Tracking timescales of short-term precursors to large basaltic fissure eruptions via Fe–Mg diffusion in olivine: EPSL, v. 439, p. 58-70.

Harvey, J., König, S., and Luguet, A., 2015, The effects of melt depletion and metasomatism on highly siderophile and strongly chalcophile elements: S-Se-Te-Re-PGE systematics of peridotite xenoliths from Kilbourne Hole, New Mexico: Geochimica et Cosmochimica Acta, v. 166, p. 210-233.

Harvey, J., Yoshikawa, M., Hammond, S. J., and Burton, K. W., 2012, Deciphering the trace element characteristics in Kilbourne Hole peridotite xenoliths: melt–rock interaction and metasomatism beneath the Rio Grande Rift, SW USA: Journal of Petrology, v. 53, no. 8, p. 1709-1742.

Holness, M. B., Farr, R., and Neufeld, J. A., 2017, Crystal settling and convection in the Shiant Isles Main Sill: Contributions to Mineralogy and Petrology, v. 172, no. 1, p. 7.

Holtzman, B., Kohlstedt, D., Zimmerman, M., Heidelbach, F., Hiraga, T., and Hustoft, J., 2003, Melt segregation and strain partitioning: implications for seismic anisotropy and mantle flow: Science, v. 301, no. 5637, p. 1227-1230.

Huang, F., Zhang, Z., Lundstrom, C. C., and Zhi, X., 2011, Iron and magnesium isotopic compositions of peridotite xenoliths from Eastern China: Geochimica et Cosmochimica Acta, v. 75, no. 12, p. 3318-3334.

Jahanbagloo, I., 1969, X-ray diffraction study of olivine solid solution series: American Mineralogist, v. 54, no. 1-2, p. 246-+.

Jarosewich, E., Nelen, J. A., and Norberg, J. A., 1980, Reference Samples for Electron Microprobe Analysis: Geostandards Newsletter, v. 4, no. 1, p. 43-47.

Jerram, D. A., Dobson, K. J., Morgan, D. J., and Pankhurst, M. J., 2018, The Petrogenesis of Magmatic Systems: Using Igneous Textures to Understand Magmatic Processes, *in* Burchardt, S., ed., Volcanic and Igneous Plumbing Systems, Elsevier, p. 191-229.

Jerram, D. A., Mock, A., Davis, G. R., Field, M., and Brown, R. J., 2009, 3D crystal size distributions: A case study on quantifying olivine populations in kimberlites: Lithos, v. 112, Supplement 1, no. 0, p. 223-235.

Kahl, M., Chakraborty, S., Costa, F., and Pompilio, M., 2011, Dynamic plumbing system beneath volcanoes revealed by kinetic modeling, and the connection to monitoring data: An example from Mt. Etna: Earth and Planetary Science Letters, v. 308, no. 1-2, p. 11-22.

Kahl, M., Chakraborty, S., Costa, F., Pompilio, M., Liuzzo, M., and Viccaro, M., 2013, Compositionally zoned crystals and real-time degassing data reveal changes in magma transfer dynamics during the 2006 summit eruptive episodes of Mt. Etna: Bulletin of Volcanology, v. 75, no. 2, p. 1-14.

Ketcham, R. A., 2005, Computational methods for quantitative analysis of three-dimensional features in geological specimens: Geosphere, v. 1, no. 1, p. 32-41.

Ketcham, R. A., and Carlson, W. D., 2001, Acquisition, optimization and interpretation of X-ray computed tomographic imagery: applications to the geosciences: Computers & Geosciences, v. 27, no. 4, p. 381-400.

Kile, D. E., 2009, The universal stage: The past, present, and future of a mineralogical research instrument: Geochemical News, v. 140, no. 8.

Leber, A. W., Knez, A., Becker, A., Becker, C., von Ziegler, F., Nikolaou, K., Rist, C., Reiser, M., White, C., Steinbeck, G., and Boekstegers, P., 2004, Accuracy of multidetector spiral computed tomography in identifying and differentiating the composition of coronary atherosclerotic plaques. A comparative study with intracoronary ultrasound.: Journal of the American College of Cardiology, v. 43, no. 7, p. 1241-1247.

Lemelle, L., Simionovici, A., Truche, R., Rau, C., Chukalina, M., and Gillet, P., 2004, A new nondestructive X-ray method for the determination of the 3D mineralogy at the micrometer scale: American Mineralogist, v. 89, no. 4, p. 547-553.

Lin, M., 2007, CrossHair v1.1.

Lin, Q., Neethling, S., Courtois, L., Dobson, K., and Lee, P., 2016, Multi-scale quantification of leaching performance using X-ray tomography: Hydrometallurgy, v. 164, p. 265-277.

Liu, X., Yu, L., Primak, A. N., and McCollough, C. H., 2009, Quantitative imaging of element composition and mass fraction using dual-energy CT: Three-material decomposition: Medical Physics, v. 36, no. 5, p. 1602-1609.

Ma, L., Taylor, K. G., Lee, P. D., Dobson, K. J., Dowey, P. J., and Courtois, L., 2016, Novel 3D centimetre-to nano-scale quantification of an organic-rich mudstone: The Carboniferous Bowland Shale, Northern England: Marine and Petroleum Geology, v. 72, p. 193-205.

Macente, A., Fusseis, F., Menegon, L., Xianghui, X., and John, T., 2017, The strain-dependent spatial evolution of garnet in a high-pressure ductile shear zone from the Western Gneiss Region (Norway): a synchrotron X-ray microtomography study: Journal of Metamorphic Geology.

Marteau, J., Gibert, D., Lesparre, N., Nicollin, F., Noli, P., and Giacoppo, F., 2012, Muons tomography applied to geosciences and volcanology: Nuclear Instruments and Methods in Physics Research Section A: Accelerators, Spectrometers, Detectors and Associated Equipment, v. 695, no. Supplement C, p. 23-28.

McDonald, S., Reischig, P., Holzner, C., Lauridsen, E., Withers, P., Merkle, A., and Feser, M., 2015, Non-destructive mapping of grain orientations in 3D by laboratory X-ray microscopy: Scientific Reports, v. 5.

Mizukami, T., Wallis, S. R., and Yamamoto, J., 2004, Natural examples of olivine lattice preferred orientation patterns with a flow-normal a-axis maximum: Nature, v. 427, no. 6973, p. 432.

Mock, A., and Jerram, D. A., 2005, Crystal Size Distributions (CSD) in Three Dimensions: Insights from the 3D Reconstruction of a Highly Porphyritic Rhyolite: Journal of Petrology, v. 46, no. 8, p. 1525-1541.

Morgan, D. J., and Jerram, D. A., 2006, On estimating crystal shape for crystal size distribution analysis: Journal of Volcanology and Geothermal Research, v. 154, no. 1-2, p. 1-7.

Nakashima, Y., 2000, The use of X-ray CT to measure diffusion coefficients of heavy ions in water-saturated porous media: Engineering Geology, v. 56, no. 1, p. 11-17.

Pankhurst, M. J., Dobson, K. J., Morgan, D. J., Loughlin, S. C., Thordarson, T., Courtios, L., and Lee, P. D., 2014, Directly monitoring the magmas fuelling volcanic eruptions in near-real-time using X-ray micro-computed tomography: Journal of Petrology, v. 55, no. 3, p. 671-684.

Pankhurst, M. J., Morgan, D. J., Thordarson, T., and Loughlin, S. C., 2018a, Magmatic crystal records in time, space, and process, causatively linked with volcanic unrest: Earth and Planetary Science Letters, v. 493, p. 231-241.

Pankhurst, M. J., Fowler, R., Courtois, L., Nonni, S., Zuddas, F., Atwood, R. C., Davis, G. R., and Lee, P. D., 2018b, Enabling three-dimensional densitometric measurements using laboratory source X-ray micro-computed tomography: SoftwareX, v. 7, p. 115-121.

Pankhurst, M. J., Walshaw, R., and Morgan, D. J., 2017, Major Element Chemical Heterogeneity in Geo2 Olivine Microbeam Reference Material: A Spatial Approach to Quantifying Heterogeneity in Primary Reference Materials: Geostandards and Geoanalytical Research, v. 41, no. 1, p. 85-91.

Philpotts, A. R., Brustman, C. M., Shi, J., Carlson, W. D., and Denison, C., 1999, Plagioclase-chain networks in slowly cooled basaltic magma: American Mineralogist, v. 84, no. 11-12, p. 1819-1829.

Pistone, M., Caricchi, L., Fife, J. L., Mader, K., and Ulmer, P., 2015, In situ X-ray tomographic microscopy observations of vesiculation of bubble-free and bubble-bearing magmas: Bulletin of Volcanology, v. 77, no. 12, p. 108.

Poldervaart, A., 1950, Correlation of physical properties and chemical composition in the plagioclase, olivine, and orthopyroxene series: American Mineralogist, v. 35, no. 11-1, p. 1067-1079.

Ramachandran, G., and Lakshminarayanan, A., 1971, Three-dimensional reconstruction from radiographs and electron micrographs: application of convolutions instead of Fourier transforms: Proceedings of the National Academy of Sciences, v. 68, no. 9, p. 2236-2240.

Rasband, W. S., 2015, ImageJ: Bethesda, Maryland, USA, 1997-2015, US National Institutes of Health.

Reyes-Dávila, G. A., Arámbula-Mendoza, R., Espinasa-Pereña, R., Pankhurst, M. J., Navarro-Ochoa, C., Savov, I., Vargas-Bracamontes, D. M., Cortés-Cortés, A., Gutiérrez-Martínez, C., Valdés-González, C., Domínguez-Reyes, T., González-Amezcua, M., Martínez-Fierros, A., Ramírez-Vázquez, C. A., Cárdenas-González, L., Castañeda-Bastida, E., Vázquez Espinoza de los Monteros, D. M., Nieto-Torres, A., Campion, R., Courtois, L., and Lee, P. D., 2016, Volcán de Colima dome collapse of July, 2015 and associated pyroclastic density currents: Journal of Volcanology and Geothermal Research, v. 320, p. 100-106.

Reyes, F., Lin, Q., Udoudo, O., Dodds, C., Lee, P., and Neethling, S., 2017, Calibrated X-ray micro-tomography for mineral ore quantification: Minerals Engineering, v. 110, p. 122-130.

Rivers, M., 1998, Tutorial introduction to X-ray computed microtomography data processing: University of Chicago.

Rudraswami, N., Prasad, M. S., Jones, R., and Nagashima, K., 2016, In situ oxygen isotope compositions in olivines of different types of cosmic spherules: An assessment of relationships to chondritic particles: Geochimica et Cosmochimica Acta, v. 194, p. 1-14.

Shea, T., Costa, F., Krimer, D., and Hammer, J. E., 2015, Accuracy of timescales retrieved from diffusion modeling in olivine: A 3D perspective: American Mineralogist, v. 100, p. 2026-2042.

Sigmundsson, F., Hreinsdóttir, S., Hooper, A., Árnadóttir, T., Pedersen, R., Roberts, M. J., Óskarsson, N., Auriac, A., Decriem, J., Einarsson, P., Geirsson, H., Hensch, M., Ófeigsson, B. G., Sturkell, E., Sveinbjörnsson, H., and Feigl, K. L., 2010, Intrusion triggering of the 2010 Eyjafjallajökull explosive eruption: Nature, v. 468, no. 7322, p. 426-432.

Sio, C. K. I., Dauphas, N., Teng, F.-Z., Chaussidon, M., Helz, R. T., and Roskosz, M., 2013, Discerning crystal growth from diffusion profiles in zoned olivine by in situ Mg–Fe isotopic analyses: Geochimica et Cosmochimica Acta, v. 123, p. 302-321.

Sorby, H. C., 1858, On the microscopical, structure of crystals, indicating the origin of minerals and rocks: Quarterly Journal of the Geological Society, v. 14, no. 1-2, p. 453-500.

Sparks, S. R. J., Sigurdsson, H., and Wilson, L., 1977, Magma mixing: a mechanism for triggering acid explosive eruptions: Nature, v. 267, no. 5609, p. 315-318.

Suuronen, J.-P., and Sayab, M., 2018, 3D nanopetrography and chemical imaging of datable zircons by synchrotron multimodal X-ray tomography: Scientific Reports, v. 8, no. 1, p. 4747.

Thomson, A., and Maclennan, J., 2013, The Distribution of Olivine Compositions in Icelandic Basalts and Picrites: Journal of Petrology, v. 54, no. 4, p. 745-768.

Vinet, N., and Higgins, M. D., 2011, What can crystal size distributions and olivine compositions tell us about magma solidification processes inside Kilauea Iki lava lake, Hawaii?: Journal of Volcanology and Geothermal Research, v. 208, no. 3–4, p. 136-162.

Vo, N. T., Drakopoulos, M., and Atwood, R. C., in prep, Superior techniques for eliminating ring artifacts in X-ray micro-tomography.

Vo, N. T., Drakopoulos, M., Atwood, R. C., and Reinhard, C., 2014, Reliable method for calculating the center of rotation in parallel-beam tomography: Optics express, v. 22, no. 16, p. 19078-19086.

Wang, H., Cai, B., Pankhurst, M. J., Zhou, T., Kashyap, Y., Atwood, R., Le Gall, N., Lee, P., Drakopoulos, M., and Sawhney, K., in press, X-ray phase-contrast imaging with engineered porous materials over 50 keV: Journal of Synchrotron Radiation.

Wang, H., Kashyap, Y., and Sawhney, K., 2016a, From synchrotron radiation to lab source: advanced speckle-based X-ray imaging using abrasive paper: Scientific reports, v. 6.

-, 2016b, Quantitative X-ray dark-field and phase tomography using single directional speckle scanning technique: Applied Physics Letters, v. 108, no. 12, p. 124102.

Whitney, D. L., and Evans, B. W., 2010, Abbreviations for names of rock-forming minerals: American Mineralogist, v. 95, no. 1, p. 185-187.

Winkler, B., Knorr, K., Kahle, A., Vontobel, P., Lehmann, E., Hennion, B., and Bayon, G., 2002, Neutron imaging and neutron tomography as non-destructive tools to study bulk-rock samples: European Journal of Mineralogy, v. 14, no. 2, p. 349-354.

Yue, S., Lee, P. D., Poologasundarampillai, G., and Jones, J. R., 2011, Evaluation of 3-D bioactive glass scaffolds dissolution in a perfusion flow system with X-ray microtomography: Acta Biomaterialia, v. 7, no. 6, p. 2637-2643.

Tables

Table 1. Description, source, and position of olivine sample discs arranged in a stack and scanned in XMT systems.

Position of disc in stack (see Fig. 2)	Sample description	Source/reference
1	Legacy crystals cut from grain mounts	Pankhurst et al. (2014)
2*	+1 mm sized crystals from the 2010 flank eruption of Eyjafjallajökull (Fimmvörðuháls: F07a above b).	T. Thordarson
3	Killbourne Hole Peridotite olivine.	Harvey et al. (2012)
4	Háleyjarbunga lava shield (picrite) olivine.	G. Fitton/T. Thordarson
5	Star-1 (alkali basalt; Papua New Guinea).	M. Turner/I. Smith
6	Green Sand Beach (Hawaii).	G. Fitton
7*	San Carlos Forsterite.	J. Harvey
8	Rockport Fayalite.	Natural History Museum, London, UK (BM.1985, MI8988)
9	Eyjafjallajökull Summit eruption (2010, Iceland) E60: b above a.	T. Thordarson

**Indicates samples used for primary calibration here, the other samples were not analysed by EPMA (i.e. cut ground and polished). Instead, they were retained to be used as internal reference materials in subsequent work.*

Table 2. Electron Probe Microanalysis secondary reference material results. Individual oxide results are accurate within 2σ of accepted values. Note the precision on major oxides used to calculate Fo content: FeO, MgO and MnO (Mn was included in all Fo calculations due to its comparatively high abundance in the fayalite sample). The exception is SiO_2, which is known to give inferior results in the type specimen. Since the Mg and Fe content dominate the attenuation contrast in the solid solution of interest here, no added uncertainty is ascribed to the data.

Springwater Meteorite olivine

Oxide	As secondary RM		Accepted value
	(n=44)		(Jarosewich et al., 1980)
	wt %	2σ	wt %
SiO_2	39.76	0.31	38.95
TiO_2	0.08	0.04	nr
Al_2O_3	bd	na	nr
Cr_2O_3	0.04	0.02	0.02
FeO	16.64	0.23	16.62
MnO	0.31	0.02	0.3
MgO	43.65	0.42	43.58
CaO	bd		nr
Total	100.21	0.74	99.47
Forsterite %*	82.38	±0.25	82.11

bd = below detection, na = not applicable, nr = not reported

*calculated using Fe, Mg and Mn as per all EPMA calculations presented here

Table 3. Crystal core Fo content, calculated density, and image data.

Crystal core	Fo*	Density**		Polychromatic data		Monochromatic data	
		g/cm^3	5% error	Intensity (16-bit)	2σ	u (53 kV)	2σ
ol3†	75.03	3.55	0.18	12819	61	1.43	0.09
ol4	76.29	3.54	0.18	12732	74	1.38	0.11
ol6	75.22	3.55	0.18	12816	69	1.44	0.11
ol7	78.18	3.52	0.18	12561	105		0.00
ol8	79.92	3.50	0.17	12571	82	1.29	0.09
ol9	79.75	3.50	0.17	12571	67	1.29	0.10
ol10	76.28	3.54	0.18	12789	70		0.00
ol11	78.37	3.51	0.18	12695	61	1.36	0.09
ol12	80.54	3.49	0.17	12491	62	1.30	0.09
ol13	80.73	3.49	0.17		84		0.00
ol15	79.86	3.50	0.17	12547	59	1.29	0.10
ol16	85.70	3.43	0.17	12139	172	1.13	0.11
ol17	78.45	3.51	0.18	12634	77	1.38	0.09
ol18	73.96	3.56	0.18		155	1.48	0.09
ol19	74.09	3.56	0.18	12768	67	1.45	0.12
ol20	74.03	3.56	0.18	12793	66	1.46	0.12
ol21	87.11	3.42	0.17	12172	65	1.13	0.09
ol22	81.53	3.48	0.17	12380	138	1.28	0.10
ol23	86.19	3.43	0.17	12196	72	1.16	0.08
ol24	77.58	3.52	0.18	12604	85	1.36	0.08
ol25	80.36	3.49	0.17	12504	65	1.32	0.12
ol26	80.50	3.49	0.17	12500	62	1.32	0.09
ol27	83.29	3.46	0.17		67		0.00
ol28	87.04	3.42	0.17	12144	60	1.13	0.09
ol29	78.53	3.51	0.18	12595	64	1.32	0.08

ol30	79.45	3.50	0.18	12532	71	1.34	0.12
ol31	78.08	3.52	0.18	12595	85	1.39	0.11
ol32	75.92	3.54	0.18	12745	56	1.41	0.08
ol33	73.57	3.57	0.18	12841	71	1.48	0.11
ol34	78.90	3.51	0.18	12517	88	1.32	0.10
ol35	80.10	3.49	0.17	12501	69	1.34	0.08
SC_1	90.95	3.37	0.17	11947	29	1.03	0.15
SC_2	90.92	3.37	0.17	11976	25	1.04	0.14
SC_3	90.92	3.37	0.17	11958	29	1.06	0.16
SC_4	89.10	3.39	0.17	12099	33	1.10	0.16
SC_5	90.89	3.37	0.17	11988	34	1.03	0.13
SC_6	89.08	3.39	0.17	12061	52	1.07	0.18
SC_7	90.96	3.37	0.17	11978	59	0.97	0.16
SC_9	90.93	3.37	0.17	11970	32	1.04	0.15
SC_10	89.09	3.39	0.17	12057	33	1.08	0.14
SC_11	90.87	3.37	0.17	11951	34	1.03	0.14
*average values per crystal core (see Table S2 for full results)							
**calculated from numerical mixing of Fo and Fa end-members							
†olXX are abbreviated from FMVD7_1mm_a_olXX (see Table S2)							

Figures

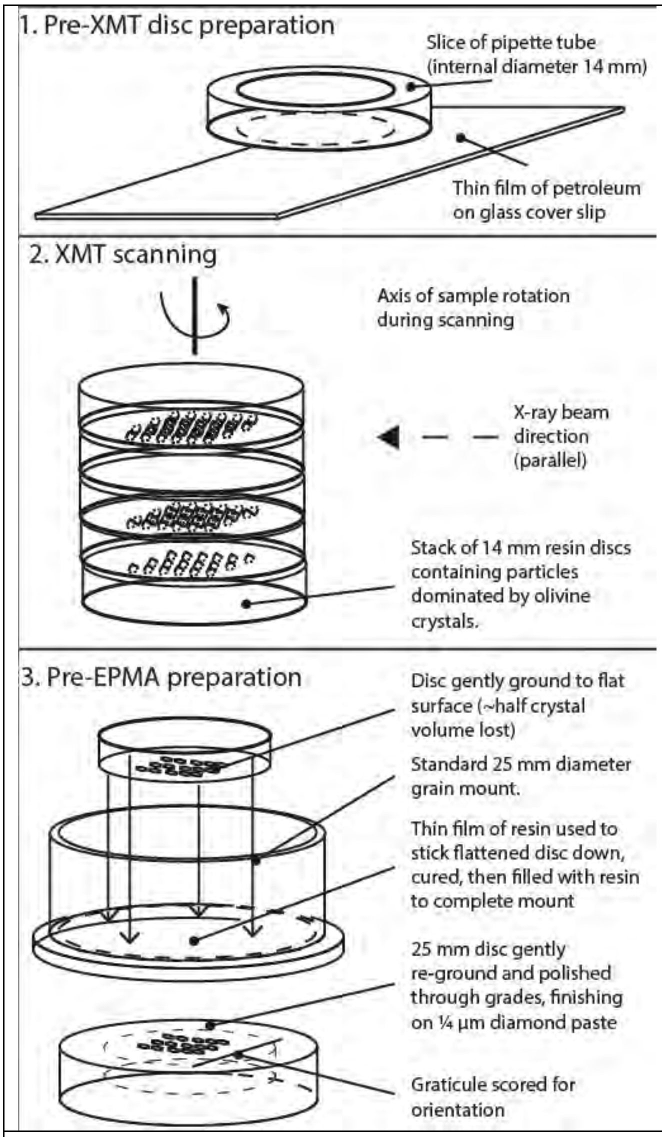

Fig. 1. **Schematic of sample preparation for integrated XMT and 2D analysis**. 1) Crystals were first set into 14 mm diamter resin discs, 2) scanned, and 3) selected discs were prepared into standard 25 mm mounts for a variety of 2D analysis.

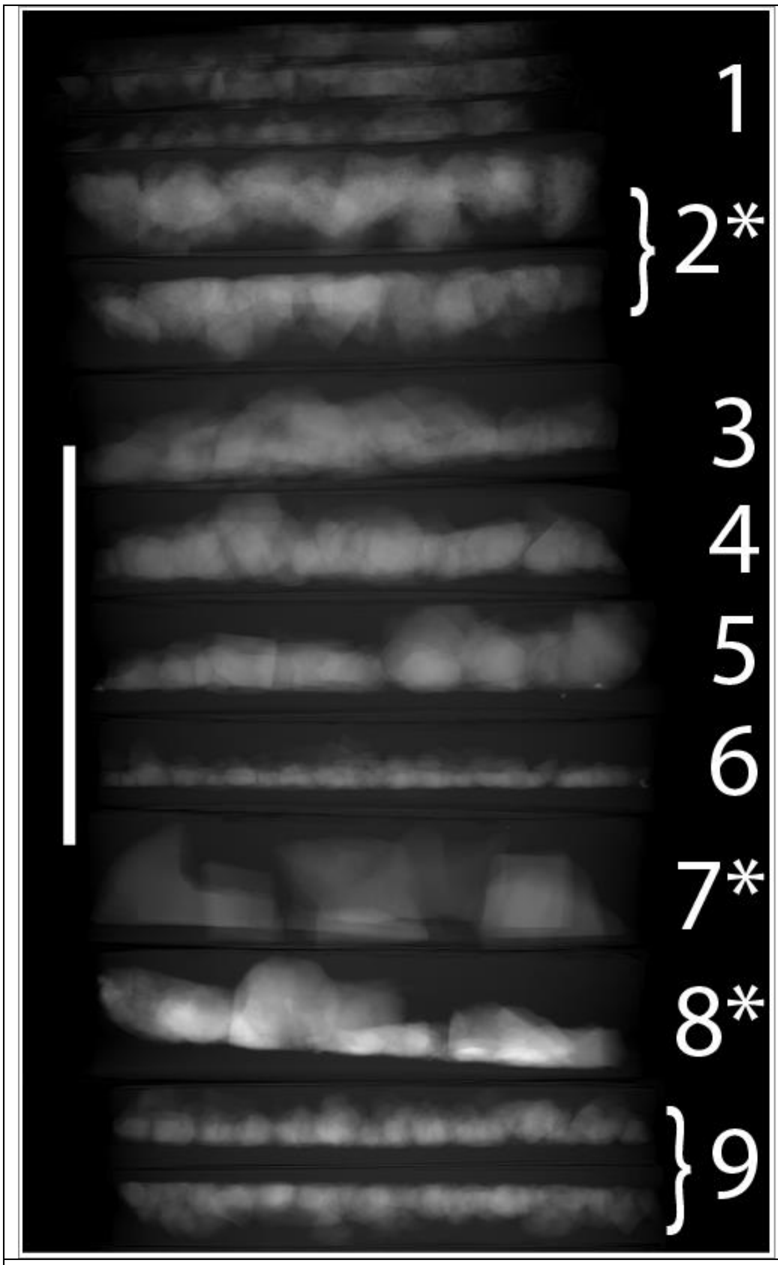

Fig. 2. **Re-projection image from reconstruction of stack.** Stack is comprised of resin discs that each contain a sample (or sample subset) of olivine. Refer to Table 1 for sample descriptions. White bar is 10 mm. *Indicates samples investigated with BSE imaging and EPMA.

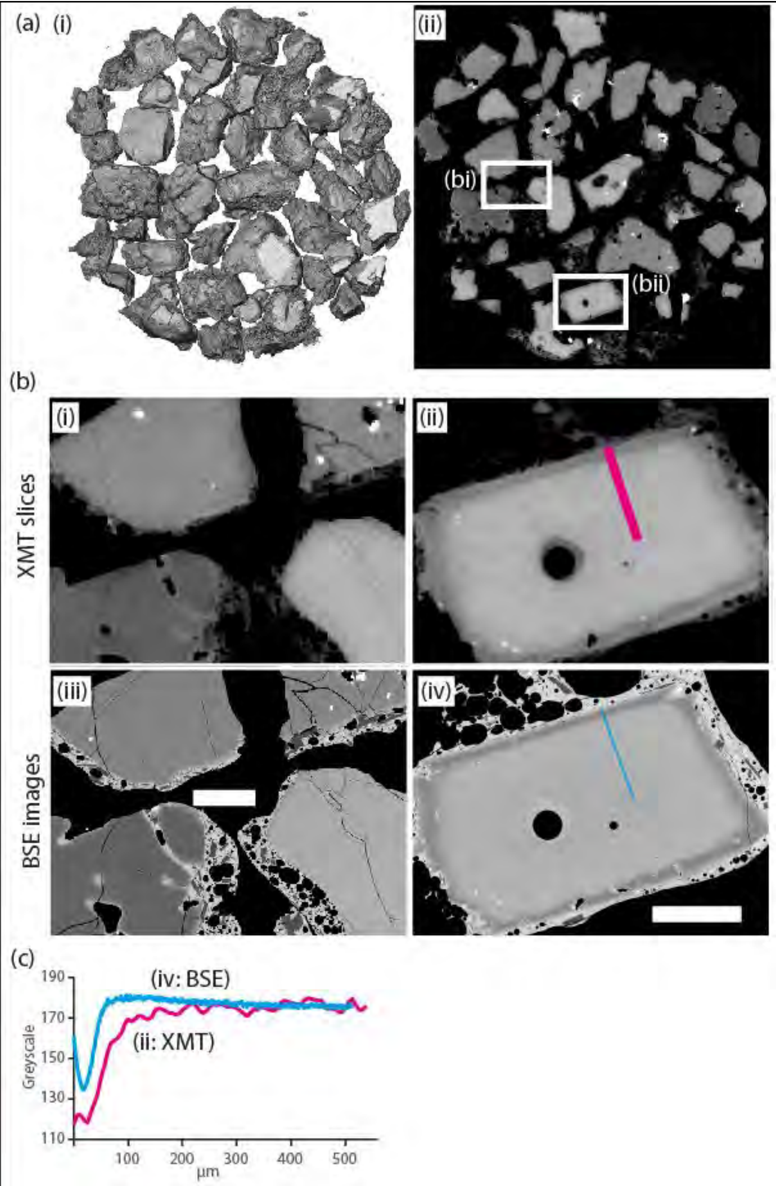

Fig. 3. Illustration of comparative 3D and 2D imaging techniques focussed upon the mineral olivine. In most cases these particles retained some vesiculated glassy matrix around the olivine crystals after being hand-picked from loose tephra. a) 3D image data from polychromatic beam, field of view = 8 mm. i) volume render of Fimmvörðuháls sample (sample 2a in stack) ii) XY orthoslice through attenuation image; insets correspond to b). b) Comparison between XMT slices (i and ii) and BSE images (iii and iv), white bars = 0.5 mm, no image filtering was performed. c) image intensity profiles from the same location in XMT and BSE data. Each line is 10 pixels wide. A qualitative match is observed: a reverse zone (darker – more Mg rich) is observed around a homogeneous core. The shape of the XMT-derived profile has a broader reverse zone than the BSE-derived profile, and the XMT profile in the core region is flatter than in the BSE.

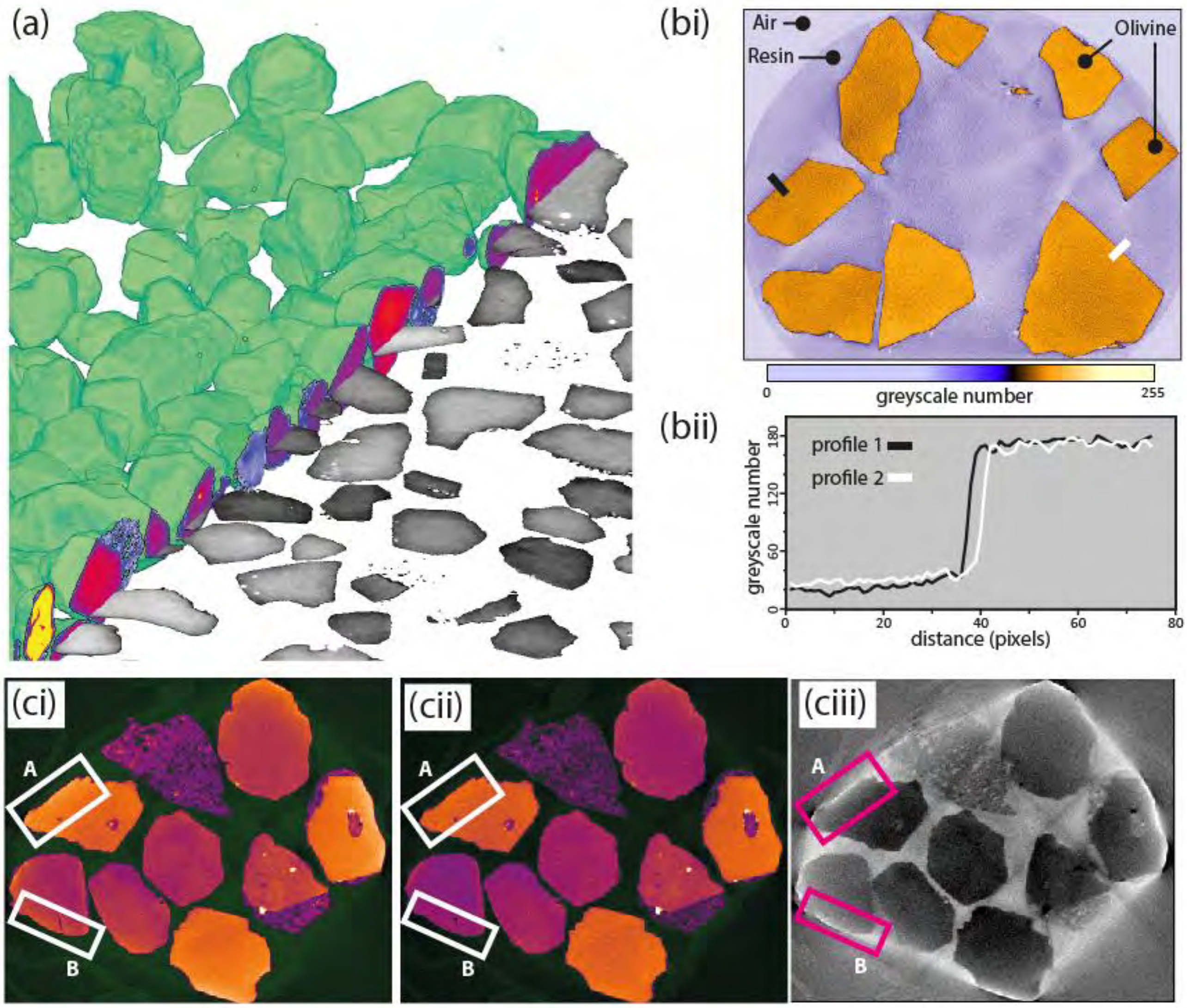

Fig. 4. **Olivine attenuation causing beam hardening at margins of grains, and its correction**. a) oblique view of olivine grains (volume render, green). Image brightness is shown as red-blue colour map in XZ cutaway and grayscale in XY, the latter approximates the 2D plane that was cut and polished (disc. b) San Carlos olivine shards. According to image brightness, each exhibit internal chemical homogeneity equivalent to that below EPMA uncertainty i) X-ray image after polychromatic beam-characterisation correction to a density value of 3.34 g cm^3, ii) profiles demonstrating step function across resin-crystal boundary. c) collection of olivine crystals with inter- and intra-crystal heterogeneity wrapped in plastic film i) before and ii) after correction to a density value of 3.45 g cm^3. iii) image cii subtracted from image ci demonstrates the approximately radial beam hardening effect is reduced, and highlights the higher sensitivity to the correction in materials with low attenuation (i.e. the film). Compare box A and B in each image. The brightening is reduced/removed from i to ii; the difference is shown in iii.

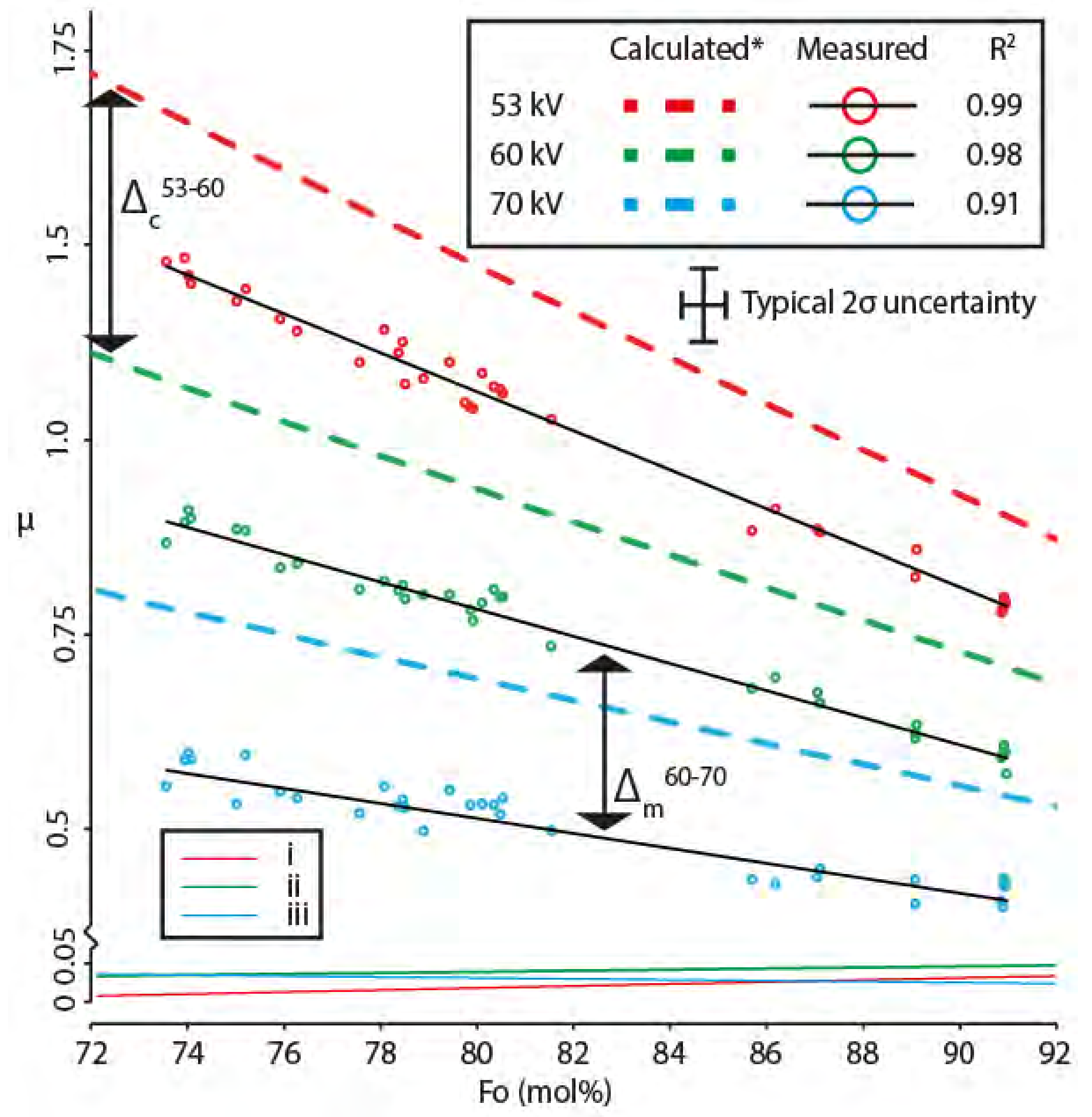

Fig. 5. **Calculated vs measured linear attenuation of the olivine solid solution from Fo$_{73-91}$.** Good linear fits are found in all datasets across Fo$_{73-91}$. There are no significant trends in the magnitude of the offset with composition or energy. Greater contrast is observed when using lower energy. At a given Fo content, the difference between the measured 53 and 60 kV values is the same as the difference between the calculated 52 and 60 kV values, within a range of 0.025 μ (line i). The same test was applied to 53 and 70 kV data (line ii) and 60 and 70 kV data (line iii), where a total range of ~0.05 μ was found, which is less than the scatter in any of the measured datasets. No significant trends in the magnitude of the offset with composition or energy are observed.

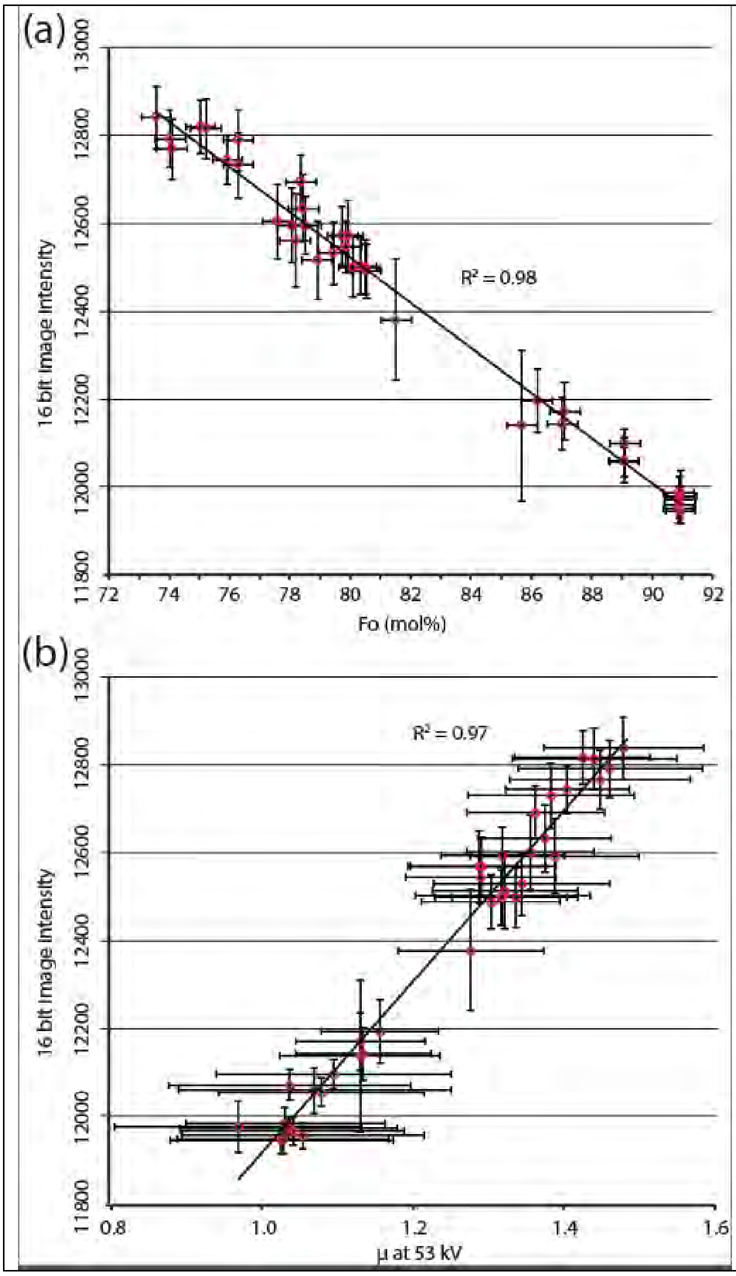

Fig. 6. **Crystal core image brightness from polychromatic X-ray source vs chemical analysis (a) and monochromatic source (b)**. Indications of accuracy and usability in a non-synchrotron setting are shown. a) A good fit to a linear regression is observed between polychromatic (laboratory scanner) scan data and EPMA. Point-specific errors reflect the image noise, two standard deviations of pixel values around the mean, at that point (no filtering was performed to generate points on this plot). b) Laboratory scanner data are observed to return higher contrast and better precision than the lowest energy monochromatic (synchrotron source) beam used.

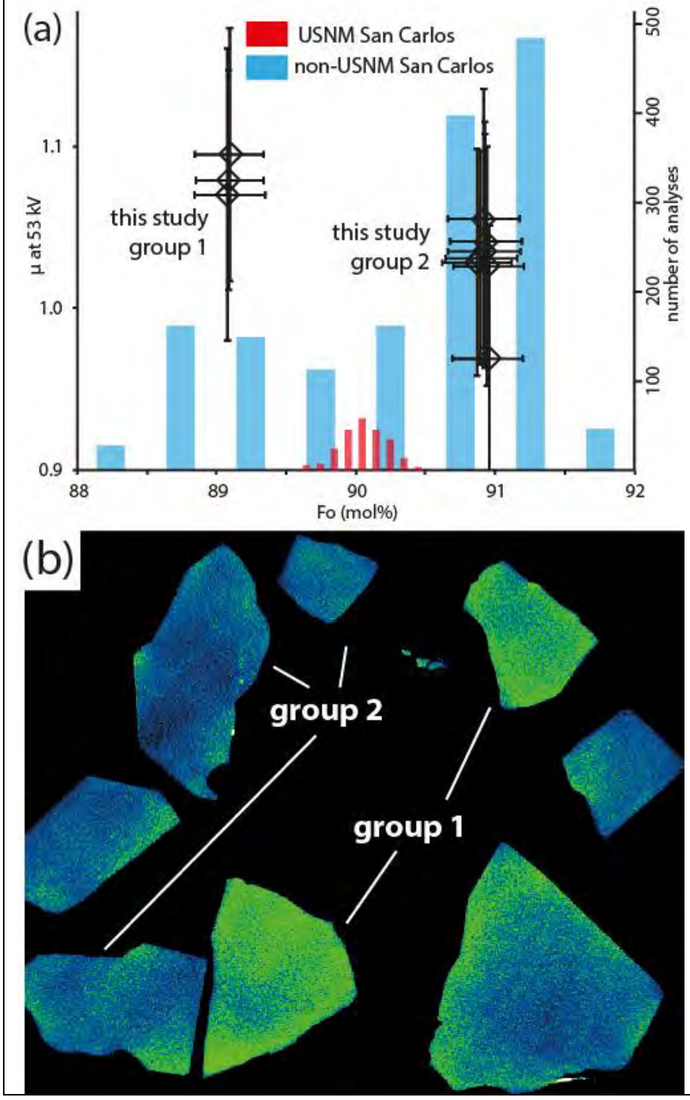

Fig. 7. **Subtle chemical heterogeneity between and within shards of a single crystal of San Carlos forsterite**. a) linear attenuation as measured using monochromatic X-rays vs. EPMA spot analyses show a distinct clustering into $Fo_{\sim 89}$ and $Fo_{\sim 91}$ groups (1 and 2 respectively). These correspond to the most common compositions of non-USNM San Carlos olivine reported by Fournelle (2011). b) laboratory-source X-ray image. Distinct differences between shards are observed. The image intensity is displayed using an arbitrary colour scheme (green = higher). The range corresponds to ~2 mol % Fo (see a), and is displayed without any filtration to provide an indication of the current signal:noise limit achievable with a modern laboratory scanner and ~1 hour scan time.

Supplementary Information

Table S1: Example calculations of mass, and linear attenuation coefficients. Mass attenuation coefficients (MAC) are calculated using the publically available XCOM database (Berger et al., 2016), from which linear attenuation coefficients (LAC) are derived using published values of density (Deer et al., 1982).

Photon energy (KeV)	Fa (p=4.39)		Fo (p=3.271)	
	MAC* cm^2/g	μ	MAC* cm^2/g	μ
40	2.17	9.51	0.43	1.39
41	2.03	8.9	0.41	1.33
42	1.9	8.34	0.39	1.28
43	1.78	7.83	0.38	1.23
44	1.68	7.36	0.36	1.18
45	1.58	6.94	0.35	1.14
46	1.49	6.55	0.34	1.1
47	1.41	6.19	0.33	1.07
48	1.33	5.86	0.32	1.03
49	1.26	5.55	0.31	1
50	1.2	5.27	0.3	0.98
51	1.14	5.01	0.29	0.95
52	1.09	4.77	0.28	0.93
53	1.04	4.54	0.28	0.9
54	0.99	4.34	0.27	0.88
55	0.94	4.14	0.26	0.86
56	0.9	3.96	0.26	0.85
57	0.86	3.8	0.25	0.83
58	0.83	3.64	0.25	0.81
59	0.8	3.49	0.24	0.8
60	0.76	3.36	0.24	0.78
61	0.74	3.23	0.24	0.77
62	0.71	3.11	0.23	0.76
63	0.68	2.99	0.23	0.75
64	0.66	2.89	0.22	0.73
65	0.63	2.79	0.22	0.72
66	0.61	2.69	0.22	0.71
67	0.59	2.6	0.22	0.71
68	0.57	2.52	0.21	0.7
69	0.56	2.44	0.21	0.69
70	0.54	2.37	0.21	0.68
71	0.52	2.29	0.21	0.67
72	0.51	2.23	0.2	0.66
73	0.49	2.16	0.2	0.66
74	0.48	2.1	0.2	0.65
75	0.47	2.05	0.2	0.64
76	0.45	1.99	0.2	0.64
77	0.44	1.94	0.19	0.63
78	0.43	1.89	0.19	0.63
79	0.42	1.84	0.19	0.62
80	0.41	1.8	0.19	0.62

*mass attenuation coefficient

Table S2: Full results from olivine EPMA. All oxide results reported in wt%. NMNH-111312-44 (Sand Carlos olivine) used as primary reference material, USNM-2566 (Springwater Meteorite olivine; see Table 2) and a pre-characterised chip of GEO2 olivine (see Pankhurst et al., 2017), used as a secondary reference materials.

SAMPLE	SiO_2	TiO_2	Al_2O_3	FeO	MnO	MgO	CaO	Cr_2O_3	TOTAL	Fo	Fa	Te
FMVD7_1mm_a_ol3	38.38	0.12	0.01	22.78	0.33	38.94	0.24	0.01	100.81	75.02	24.62	
FMVD7_1mm_a_ol3	38.41	0.11	bd	22.75	0.32	38.91	0.24	0.01	100.74	75.04	24.62	
FMVD7_1mm_a_ol4	38.72	0.10	0.01	21.82	0.29	39.80	bd	0.02	100.70	76.24	23.45	
FMVD7_1mm_a_ol4	38.70	0.10	bd	21.65	0.29	39.70	bd	0.02	100.05	76.33	23.35	
FMVD7_1mm_a_ol6	38.20	0.09	0.01	22.67	0.29	38.99	0.18	0.00	100.45	75.16	24.52	
FMVD7_1mm_a_ol6	38.12	0.10	0.02	22.50	0.28	38.94	bd	0.01	99.76	75.29	24.40	
FMVD7_1mm_a_ol7	38.89	0.09	0.01	19.86	0.30	40.71	bd	0.03	99.63	78.26	21.42	
FMVD7_1mm_a_ol7	38.94	0.11	0.01	20.06	0.29	40.72	bd	0.02	99.84	78.10	21.59	
FMVD7_1mm_a_ol8	39.11	0.10	0.02	18.84	0.26	42.52	0.47	0.03	101.34	79.87	19.85	
FMVD7_1mm_a_ol8	39.20	0.09	0.01	18.64	0.26	42.34	bd	0.03	100.25	79.97	19.75	
FMVD7_1mm_a_ol9	39.26	0.10	0.02	18.68	0.26	41.82	bd	0.03	99.72	79.74	19.98	
FMVD7_1mm_a_ol9	39.24	0.10	0.01	18.75	0.25	41.99	bd	0.02	99.97	79.76	19.98	
FMVD7_1mm_a_ol10	38.32	0.10	0.02	21.77	0.29	39.71	0.21	0.00	100.42	76.24	23.44	
FMVD7_1mm_a_ol10	38.37	0.09	0.01	21.68	0.27	39.71	bd	0.01	100.13	76.33	23.38	
FMVD7_1mm_a_ol11	38.78	0.09	0.01	19.97	0.28	41.16	0.43	0.02	100.74	78.37	21.33	
FMVD7_1mm_a_ol11	38.77	0.11	0.01	20.00	0.27	41.22	0.33	0.02	100.73	78.38	21.34	
FMVD7_1mm_a_ol12	39.21	0.10	0.02	18.18	0.24	42.68	bd	0.02	100.04	80.51	19.23	
FMVD7_1mm_a_ol12	39.22	0.10	0.01	18.11	0.24	42.70	0.23	0.03	100.64	80.57	19.18	
FMVD7_1mm_a_ol13	38.94	0.11	0.01	17.92	0.24	42.77	bd	0.03	99.62	80.76	18.98	
FMVD7_1mm_a_ol13	39.09	0.10	0.01	17.96	0.24	42.68	0.28	0.02	100.39	80.70	19.05	
FMVD7_1mm_a_ol15	39.10	0.09	0.01	18.72	0.23	42.10	bd	0.02	99.89	79.84	19.91	
FMVD7_1mm_a_ol15	39.28	0.10	0.01	18.67	0.25	42.17	bd	0.03	100.02	79.89	19.84	
FMVD7_1mm_a_ol16	39.83	0.10	0.03	13.69	0.17	46.29	0.37	0.06	100.55	85.62	14.20	
FMVD7_1mm_a_ol16	39.91	0.07	0.03	13.50	0.18	46.30	bd	0.06	99.89	85.78	14.03	
FMVD7_1mm_a_ol17	38.85	0.10	bd	19.85	0.26	40.99	bd	0.01	99.50	78.42	21.30	
FMVD7_1mm_a_ol17	38.92	0.10	0.01	19.78	0.28	41.08	bd	0.01	99.71	78.49	21.21	
FMVD7_1mm_a_ol18	38.13	0.09	bd	23.51	0.34	38.06	0.77	0.00	100.90	73.98	25.64	
FMVD7_1mm_a_ol18	38.20	0.09	0.00	23.53	0.33	37.99	0.18	0.00	100.33	73.94	25.69	
FMVD7_1mm_a_ol19	38.21	0.10	0.01	23.42	0.34	38.21	bd	0.01	99.73	74.13	25.49	
FMVD7_1mm_a_ol19	38.14	0.08	0.01	23.48	0.35	38.15	0.05	bd	100.24	74.05	25.57	
FMVD7_1mm_a_ol20	37.87	0.09	bd	23.46	0.32	38.11	bd	bd	99.30	74.06	25.58	
FMVD7_1mm_a_ol20	38.12	0.10	0.01	23.49	0.34	38.04	bd	0.00	99.65	73.99	25.63	

FMVD7_1mm_a_ol21	40.14	0.07		0.03	12.28	0.15	47.13	bd	0.06	99.67	87.11	12.74	
FMVD7_1mm_a_ol21	40.11	0.07		0.02	12.30	0.17	47.27	0.21	0.05	100.20	87.11	12.71	
FMVD7_1mm_a_ol22	39.34	0.09		0.02	17.26	0.23	43.33	bd	0.03	100.02	81.54	18.22	
FMVD7_1mm_a_ol22	39.41	0.10		0.01	17.25	0.24	43.31	bd	0.02	99.87	81.53	18.21	
FMVD7_1mm_a_ol23	40.04	0.09		0.02	13.01	0.17	46.22	bd	0.06	99.15	86.21	13.61	
FMVD7_1mm_a_ol23	40.16	0.07		0.02	13.08	0.16	46.34	bd	0.06	99.21	86.18	13.65	
FMVD7_1mm_a_ol24	38.72	0.10		0.01	20.55	0.29	40.44	bd	0.02	99.66	77.57	22.12	
FMVD7_1mm_a_ol24	38.68	0.09		0.01	20.53	0.29	40.46	bd	0.01	99.82	77.59	22.09	
FMVD7_1mm_a_ol25	38.97	0.09		0.00	18.24	0.24	42.48	bd	0.02	99.77	80.38	19.36	
FMVD7_1mm_a_ol25	38.97	0.08		0.01	18.30	0.25	42.51	bd	0.01	99.56	80.33	19.40	
FMVD7_1mm_a_ol26	39.06	0.08		0.02	18.12	0.24	42.43	bd	0.02	99.56	80.47	19.27	
FMVD7_1mm_a_ol26	39.00	0.09		0.01	18.05	0.26	42.46	bd	0.02	99.39	80.52	19.20	
FMVD7_1mm_a_ol27	39.33	0.08		0.02	15.61	0.21	44.42	bd	0.04	99.32	83.35	16.43	
FMVD7_1mm_a_ol27	39.54	0.09		0.02	15.73	0.22	44.41	bd	0.06	99.51	83.23	16.53	
FMVD7_1mm_a_ol28	40.18	0.07		0.03	12.33	0.16	47.12	bd	0.06	99.29	87.05	12.78	
FMVD7_1mm_a_ol28	40.30	0.07		0.03	12.33	0.17	47.07	bd	0.06	99.60	87.03	12.79	
FMVD7_1mm_a_ol29	38.95	0.08		0.01	19.89	0.27	41.20	bd	0.01	100.09	78.46	21.25	
FMVD7_1mm_a_ol29	38.95	0.10		0.02	19.76	0.28	41.27	0.43	0.01	100.82	78.59	21.10	
FMVD7_1mm_a_ol30	39.13	0.09		0.01	19.05	0.27	41.83	bd	0.02	99.81	79.42	20.29	
FMVD7_1mm_a_ol30	38.97	0.08		0.02	19.00	0.26	41.84	bd	0.03	100.18	79.48	20.24	
FMVD7_1mm_a_ol31	38.69	0.09		0.02	20.18	0.29	40.93	0.47	0.02	100.69	78.09	21.60	
FMVD7_1mm_a_ol31	38.71	0.10		0.02	20.18	0.29	40.88	bd	0.01	99.98	78.07	21.62	
FMVD7_1mm_a_ol32	38.48	0.10		0.00	22.00	0.31	39.33	bd	0.01	99.76	75.86	23.80	
FMVD7_1mm_a_ol32	38.55	0.10		0.02	21.90	0.31	39.41	0.08	0.00	100.37	75.98	23.69	
FMVD7_1mm_a_ol33	37.99	0.07		0.01	23.82	0.33	37.84	bd	0.00	99.56	73.64	26.00	
FMVD7_1mm_a_ol33	37.86	0.09		0.00	23.95	0.31	37.78	bd	0.02	99.97	73.51	26.14	
FMVD7_1mm_a_ol34	38.74	0.09		0.01	19.50	0.27	41.50	0.01	0.01	100.11	78.91	20.80	
FMVD7_1mm_a_ol34	38.71	0.09		0.01	19.50	0.28	41.46	0.62	0.02	100.69	78.89	20.81	
FMVD7_1mm_a_ol35	39.09	0.09		0.02	18.45	0.26	42.20	bd	0.02	99.44	80.09	19.64	
FMVD7_1mm_a_ol35	39.04	0.10		0.02	18.48	0.25	42.33	0.33	0.03	100.58	80.11	19.62	
RP_1	29.62	0.11		bd	66.52	2.55	0.01	0.03	0.00	98.81		96.23	3.74
RP_1r	29.63	0.13		bd	66.59	2.56	-0.01	bd	0.00	98.58		96.27	3.75
RP_2	29.64	0.12		bd	66.46	2.59	0.00	bd	0.00	98.40		96.19	3.80
RP_2r	29.49	0.10		bd	66.34	2.60	0.02	0.19	0.01	98.71		96.14	3.82
RP_3	29.59	0.12		bd	65.90	2.55	-0.01	bd	0.00	97.93		96.25	3.78
RP_3r	29.73	0.13		bd	66.27	2.55	0.01	bd	0.01	98.56		96.22	3.75
RP_4	29.64	0.12		bd	66.23	2.54	-0.01	bd	bd	98.08		96.30	3.73

RP_4r	29.71	0.12	bd	66.57	2.57	0.01	bd	0.00	98.56		96.20	3.77
RP_5	29.60	0.11	bd	66.31	2.57	0.01	bd	0.00	98.17		96.21	3.77
RP_5r	29.57	0.11	bd	66.35	2.54	bd	bd	bd	98.09		96.32	3.73
RP_6	29.76	0.12	bd	66.62	2.54	0.01	bd	0.00	98.93		96.26	3.72
RP_6r	29.79	0.09	bd	66.86	2.53	0.02	bd	0.00	98.72		96.26	3.70
RP_8	29.74	0.10	bd	66.55	2.53	0.01	bd	0.00	98.39		96.27	3.71
RP_8r	29.71	0.12	bd	66.42	2.54	0.01	bd	0.00	97.95		96.25	3.73
RP_9	29.55	0.11	bd	66.14	2.56	bd	0.05	0.00	98.37		96.22	3.77
RP_9r	29.64	0.11	bd	66.21	2.58	bd	bd	bd	98.41		96.22	3.80
RP_10	29.75	0.12	bd	66.42	2.53	0.01	bd	bd	98.58		96.25	3.72
RP_10r	29.75	0.12	bd	66.61	2.55	0.00	0.08	bd	99.07		96.27	3.73
RP_11	29.77	0.12	bd	66.62	2.54	0.03	bd	bd	98.97		96.21	3.72
RP_11r	29.76	0.13	bd	66.41	2.56	0.00	bd	0.00	98.29		96.25	3.75
RP_12	29.79	0.12	bd	66.33	2.53	0.01	bd	0.00	98.64		96.26	3.72
RP_12r	29.79	0.13	bd	66.37	2.57	bd	bd	0.00	98.80		96.26	3.78
RP_13	29.64	0.12	bd	66.25	2.54	0.01	bd	0.01	98.29		96.24	3.74
RP_13r	29.62	0.11	bd	66.15	2.56	0.01	bd	0.01	97.91		96.22	3.77
RP_14	29.79	0.13	bd	66.62	2.55	0.00	0.17	0.00	99.23		96.27	3.74
RP_14r	29.74	0.13	bd	66.64	2.49	0.01	0.17	0.01	99.16		96.32	3.64
RP_15	29.69	0.13	bd	66.35	2.59	bd	bd	0.00	98.63		96.24	3.81
RP_15r	29.79	0.13	bd	66.43	2.58	0.02	0.19	0.00	99.08		96.18	3.78
SC_1	41.20	0.08	bd	8.82	0.13	50.33	0.12	0.03	100.70	90.93	8.94	
SC_1r	41.13	0.08	bd	8.82	0.13	50.48	bd	0.03	100.32	90.96	8.91	
SC_1r2	40.98	0.07	bd	8.83	0.13	50.58	bd	0.02	100.39	90.95	8.91	
SC_2	41.05	0.08	bd	8.87	0.14	50.42	bd	0.02	100.05	90.89	8.97	
SC_2r	40.94	0.08	bd	8.83	0.14	50.52	bd	0.08	100.23	90.94	8.91	
SC_2r2	40.95	0.08	bd	8.85	0.13	50.55	bd	0.02	100.15	90.94	8.93	
SC_3	41.17	0.09	bd	8.88	0.12	50.61	bd	0.02	100.54	90.92	8.95	
SC_3r	41.19	0.09	bd	8.86	0.14	50.56	0.06	0.02	100.91	90.92	8.94	
SC_3r2	41.16	0.09	bd	8.87	0.12	50.47	bd	0.01	100.61	90.91	8.97	
SC_4	40.70	0.08	bd	10.55	0.16	49.16	bd	0.01	100.26	89.11	10.73	
SC_4r	41.19	0.10	bd	10.49	0.15	48.35	bd	0.01	100.29	89.01	10.83	
SC_4r2	40.85	0.08	bd	10.48	0.15	49.08	bd	0.02	100.53	89.17	10.68	
SC_5	41.24	0.08	bd	8.83	0.13	50.38	bd	0.02	100.13	90.92	8.94	
SC_5r	41.26	0.08	bd	8.87	0.12	50.29	bd	0.02	100.20	90.89	8.99	
SC_5r2	41.16	0.09	bd	8.91	0.14	50.53	0.00	0.03	100.85	90.87	8.99	
SC_6	41.03	0.10	bd	10.53	0.15	49.08	bd	0.02	100.60	89.12	10.72	

SC_6r	40.91	0.09	bd	10.59	0.15	49.08	bd	0.03	100.53	89.07	10.78
SC_6r2	40.97	0.09	bd	10.62	0.15	49.09	0.12	0.02	101.06	89.04	10.80
SC_7	41.18	0.08	bd	8.81	0.13	50.63	bd	0.02	100.81	90.99	8.88
SC_7r	41.18	0.08	bd	8.81	0.13	50.49	0.00	0.02	100.70	90.96	8.90
SC_7r2	41.22	0.09	bd	8.87	0.12	50.55	bd	0.04	100.65	90.92	8.95
SC_9	41.22	0.09	bd	8.87	0.14	50.54	bd	0.02	100.58	90.91	8.96
SC_9r	41.14	0.09	bd	8.85	0.14	50.49	bd	0.02	100.43	90.92	8.94
SC_9r2	41.22	0.08	bd	8.81	0.12	50.38	bd	0.03	100.24	90.95	8.92
SC_10	41.04	0.09	bd	10.59	0.15	49.07	bd	0.01	100.31	89.06	10.79
SC_10r	40.84	0.08	bd	10.55	0.16	49.16	0.17	0.01	100.97	89.10	10.73
SC_10r2	40.82	0.09	bd	10.52	0.16	48.95	bd	0.01	100.15	89.09	10.74
SC_11	41.19	0.09	bd	8.93	0.12	50.47	bd	0.01	100.44	90.86	9.02
SC_11r	41.22	0.07	bd	8.92	0.14	50.36	0.08	0.02	100.80	90.83	9.03
SC_11r2	41.08	0.09	bd	8.83	0.13	50.26	bd	0.02	100.16	90.91	8.96

r denotes repeat spot analysis, <10 µm from the original. r2 is a second repeat, also <10 µm from the original

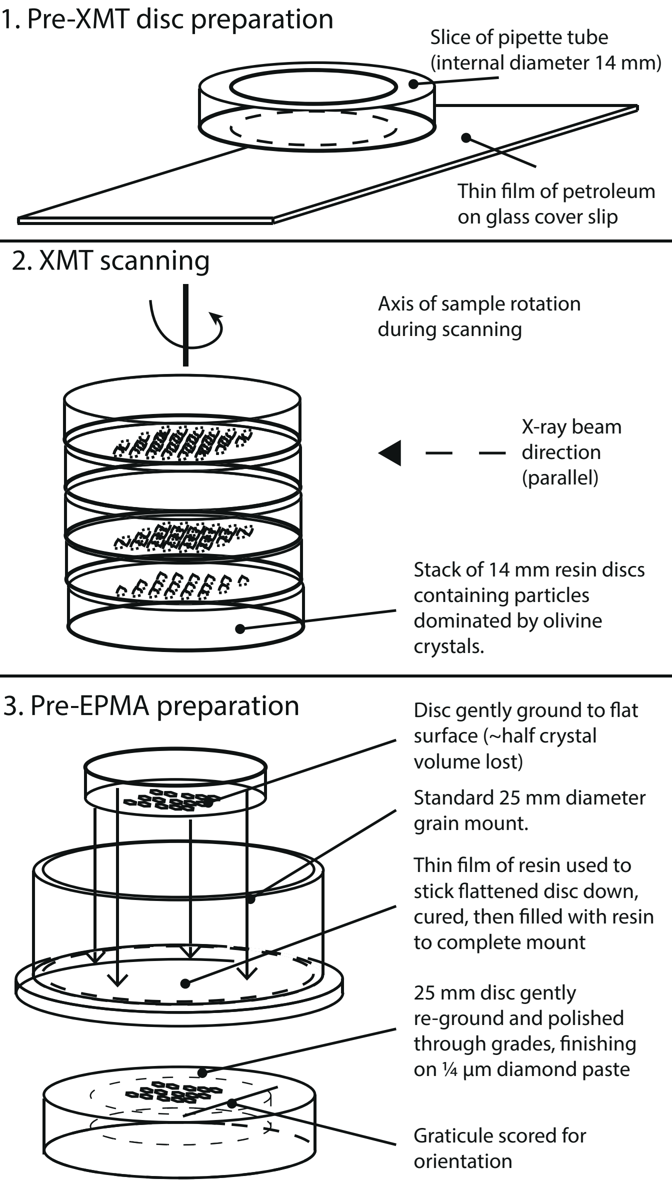
1. Pre-XMT disc preparation
Slice of pipette tube (internal diameter 14 mm)
Thin film of petroleum on glass cover slip
2. XMT scanning
Axis of sample rotation during scanning
X-ray beam direction (parallel)
Stack of 14 mm resin discs containing particles dominated by olivine crystals.
3. Pre-EPMA preparation
Disc gently ground to flat surface (~half crystal volume lost)
Standard 25 mm diameter grain mount.
Thin film of resin used to stick flattened disc down, cured, then filled with resin to complete mount
25 mm disc gently re-ground and polished through grades, finishing on ¼ µm diamond paste
Graticule scored for orientation

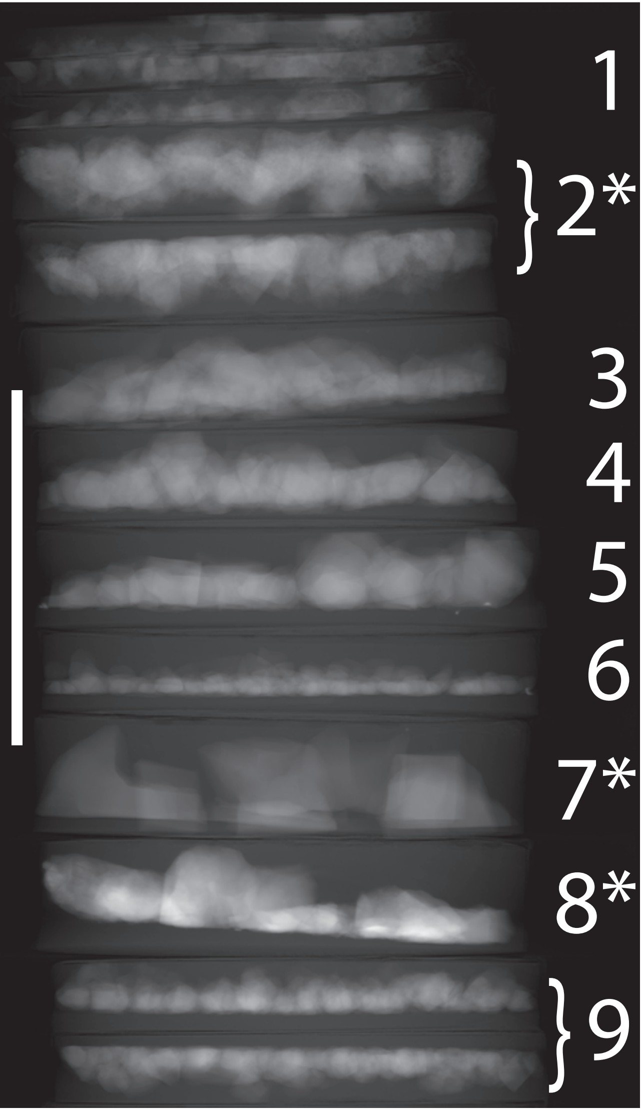
1
2*
3
4
5
6
7*
8*
9

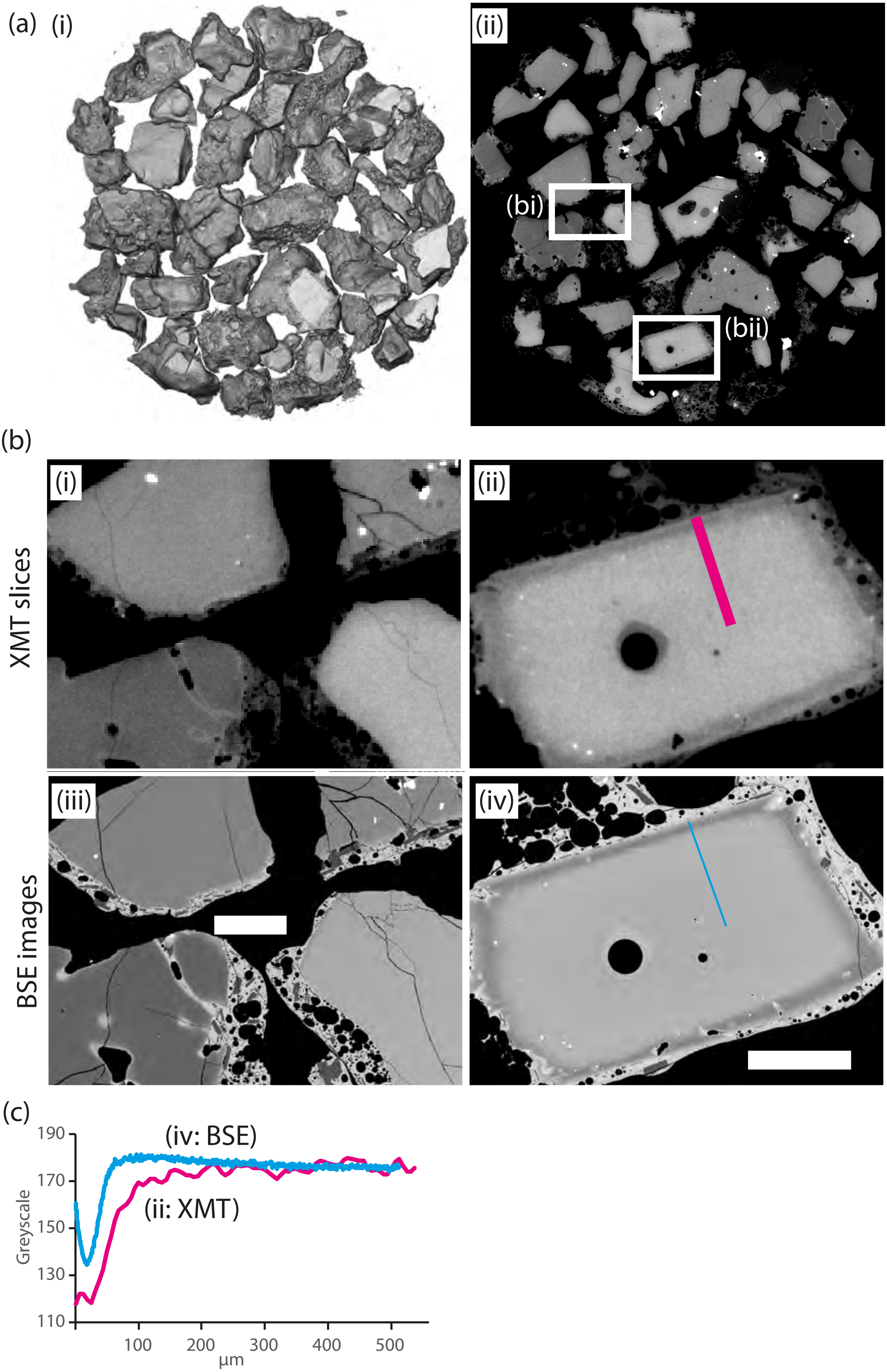
(a)
(i)
(ii)
(bi)
(bii)
(b)
XMT slices
BSE images
(i)
(ii)
(iii)
(iv)
(c)
190
170
150
130
110
Greyscale
(iv: BSE)
(ii: XMT)
100
200
300
400
500
μm

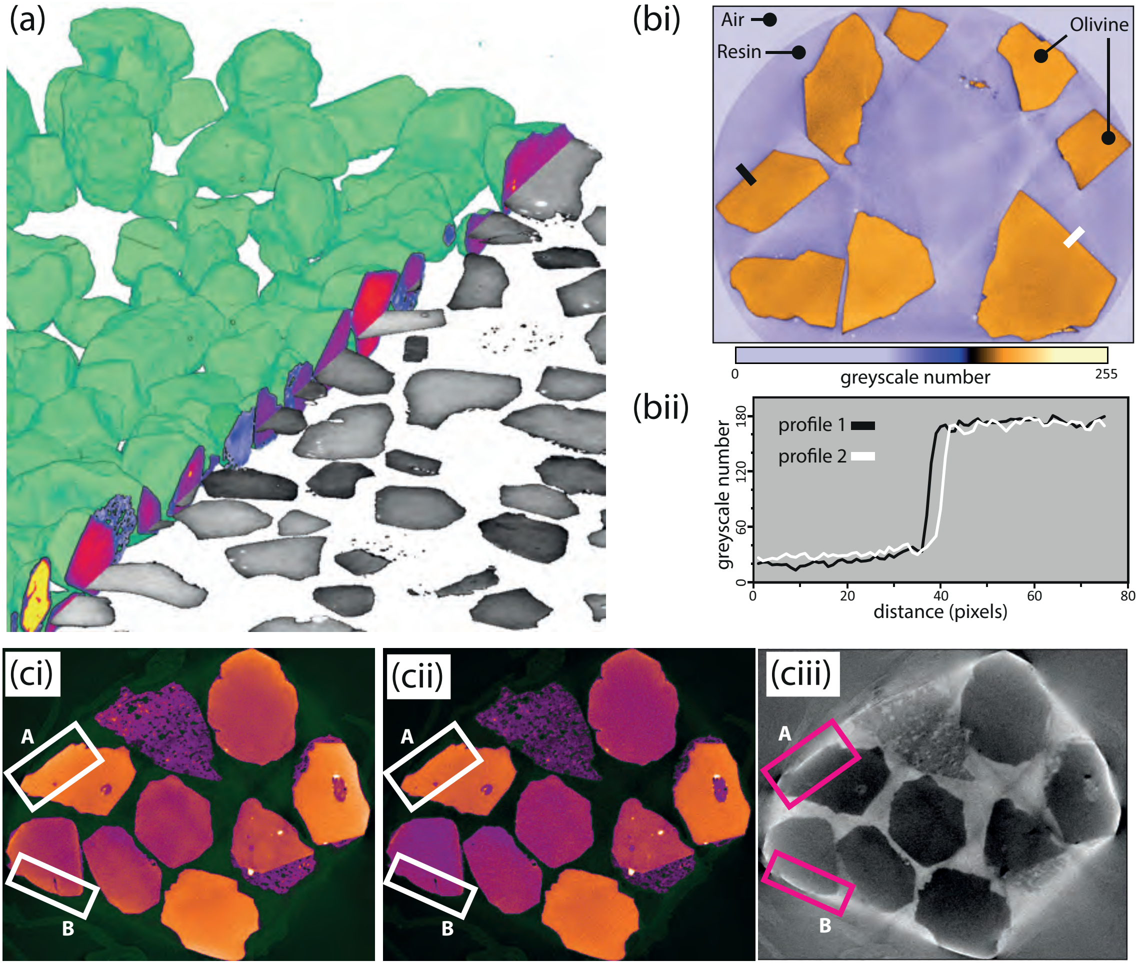
(a)
(bi)
Air
Resin
Olivine
0
greyscale number
255
(bii)
profile 1
profile 2
greyscale number
0
60
120
180
0
20
40
60
80
distance (pixels)
(ci)
A
B
(cii)
A
B
(ciii)
A
B

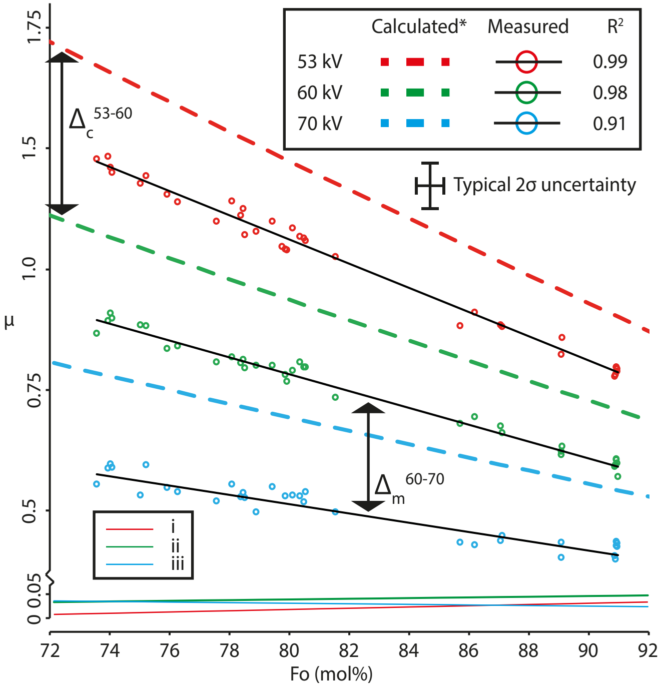
Calculated*
Measured
R²
53 kV
0.99
60 kV
0.98
70 kV
0.91
Typical 2σ uncertainty
Δc 53-60
Δm 60-70
i
ii
iii
μ
1.75
1.5
1.0
0.75
0.5
0.05
0
72
74
76
78
80
82
84
86
88
90
92
Fo (mol%)

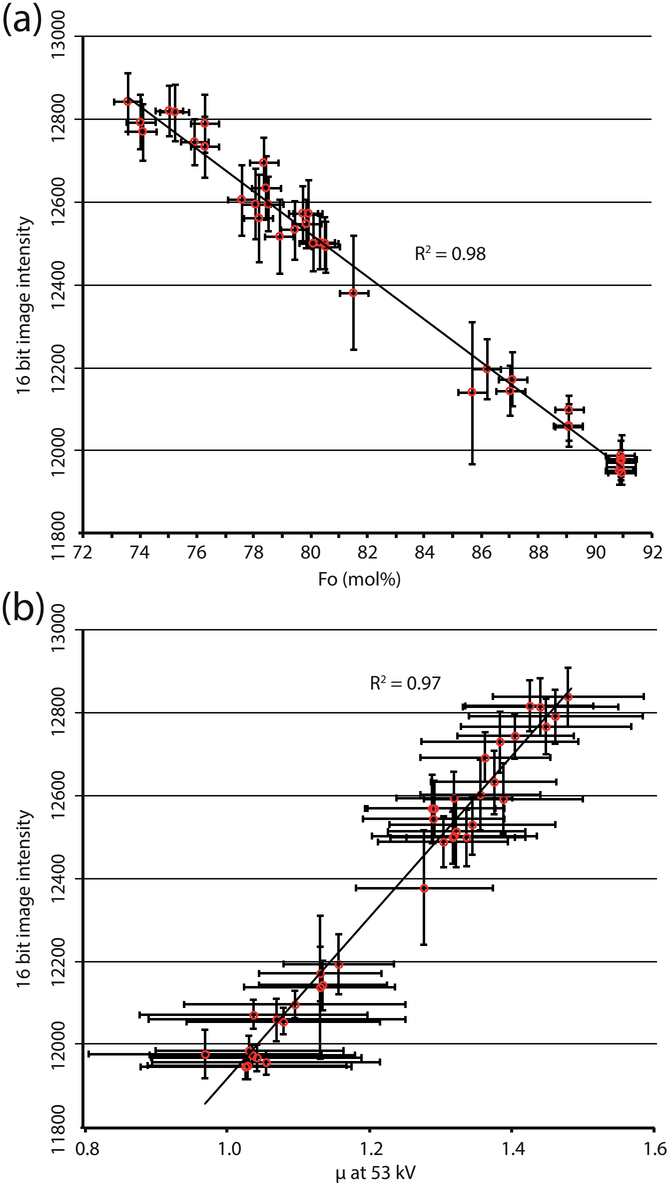
(a)
16 bit image intensity
11800
12000
12200
12400
12600
12800
13000
R² = 0.98
72
74
76
78
80
82
84
86
88
90
92
Fo (mol%)
(b)
16 bit image intensity
11800
12000
12200
12400
12600
12800
13000
R² = 0.97
0.8
1.0
1.2
1.4
1.6
μ at 53 kV

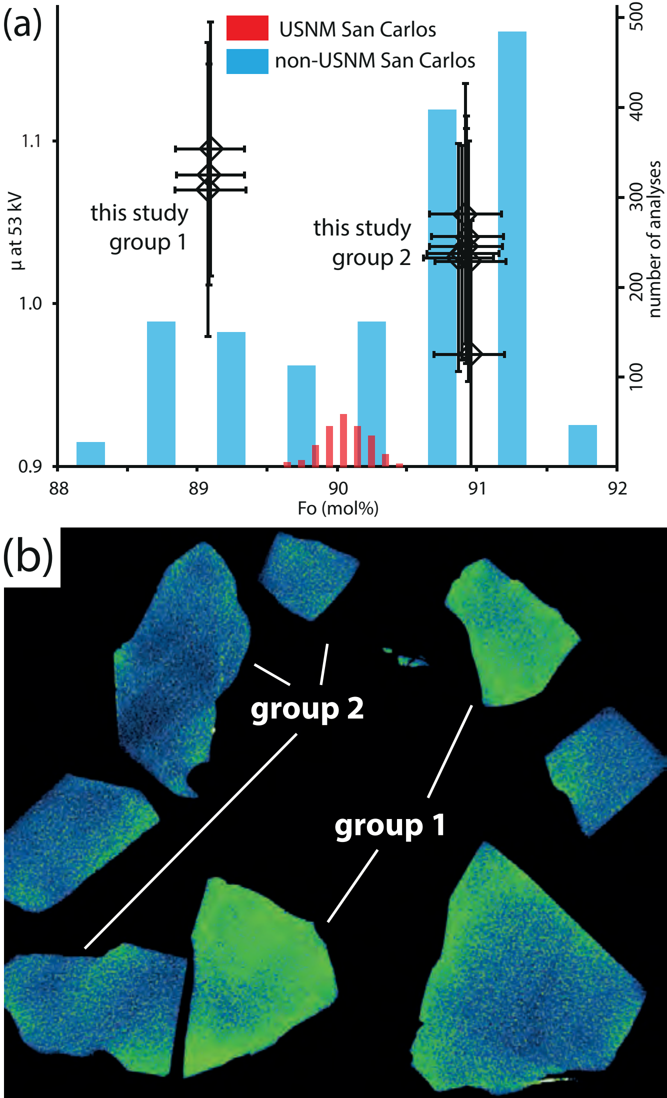
(a)
USNM San Carlos
non-USNM San Carlos
this study group 1
this study group 2
μ at 53 kV
1.1
1.0
0.9
number of analyses
500
400
300
200
100
88
89
90
91
92
Fo (mol%)
(b)
group 2
group 1

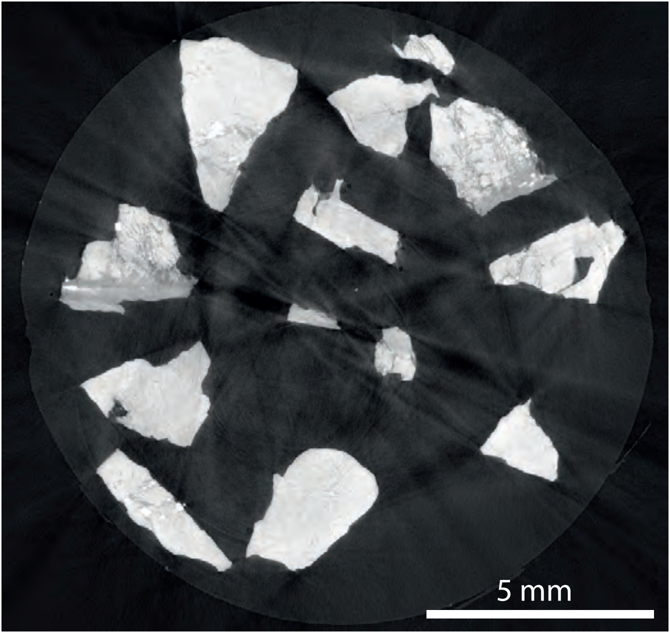
5 mm